Engineering Fracture Mechanics 78 (2011) 205–225

Contents lists available at ScienceDirect

Engineering Fracture Mechanics

journal homepage: www.elsevier.com/locate/engfracmech

Microstructural effects on ductile fracture in heterogeneous materials. Part I: Sensitivity analysis with LE-VCFEM

Daniel Paquet, Somnath Ghosh *

Department of Mechanical Engineering, The Ohio State University, 201 West 19th Avenue, Columbus, OH 43210, United States

ARTICLE INFO

Article history:
Available online 18 July 2010

Keywords:
Rate-dependent ductile fracture
Heterogeneous materials
Sensitivity analysis
LE-VCFEM

ABSTRACT

Ductile failure of heterogeneous materials, such as cast aluminum alloys and discretely reinforced aluminums or DRA's, initiates with cracking, fragmentation or interface separation of inclusions, that is followed by propagation in the matrix by a ductile mechanism of void nucleation and growth. Damage localizes in bands of intense plastic deformation between inclusions and coalesces into a macroscopic crack leading to overall failure. Ductile fracture is very sensitive to the local variations of the microstructure morphology. This is the first of a two part paper on the effect of microstructural morphology and properties on the ductile fracture in heterogeneous ductile materials. In this paper the *locally enhanced Voronoi cell finite element method* (LE-VCFEM) for rate-dependent porous elastic–viscoplastic materials is used to investigate the sensitivity of strain to failure to loading rates, microstructural morphology and material properties. A model is also proposed for strain to failure, incorporating the effects of important morphological parameters.

© 2010 Elsevier Ltd. All rights reserved.

1. Introduction

Ductile failure in metals and alloys containing heterogeneities such as particulates, fibers or precipitates, generally initiates at the heterogeneity with fragmentation or interface separation. Subsequently, the microstructural damage propagates into the matrix by mechanisms of void growth. Often, the damage localizes in bands of intense plastic deformation between heterogeneities, which subsequently coalesce into macroscopic cracks leading to complete failure. Experimental studies on ductile failure have shown strong connections between the microstructural morphology and damage nucleation and growth. A robust understanding of the influence of the microstructure on ductile fracture is essential for material design.

A variety of experimental studies have been undertaken on the influence of morphology on ductile failure, particularly related to cast aluminum alloys and DRA's [1–12]. In their studies on cast aluminum alloys, Caceres et al. [13,14,6,15–17] have shown that ductility of the Al–7%Si–0.4%Mg cast alloy depends on both the dendrite cell size and the size and shape of silicon inclusions. While these experimental studies offer good qualitative understanding, they do not quantify the influence of microstructure parameters on ductile fracture. Often, the difficulty arises with isolating the effect of individual morphological parameters like shape, size or spatial distribution [15]. Analytical and computational models have been implemented for fulfilling this need. Computational studies have been conducted to study elastic–plastic deformation and ductile failure of heterogeneous materials in [18–24]. A majority of these are unit cell models with size scales exceeding 1 μm, that use continuum micromechanics for modeling inclusions and matrix [25]. There is a paucity of image-based models that consider aspects of the real microstructural morphology, such as non-uniformities in inclusion shape, size, orientation and spatial distribution. The predictive capability of unit cell models for failure properties is very limited due to

* Corresponding author. Tel.: +1 614 292 2599; fax: +1 614 292 7369.
E-mail address: ghosh.5@osu.edu (S. Ghosh).

0013-7944/$ - see front matter © 2010 Elsevier Ltd. All rights reserved.
doi:10.1016/j.engfracmech.2010.07.009

Nomenclature

a, b	inclusion major and minor axes
d	inclusion size $d = 2\sqrt{ab}$
$\bar{d}$	inclusion normalized size $\bar{d} = d/L_{MD}$
$\mathbf{e}$	macroscopic strain tensor
E	Young's modulus
f_0	initial void volume fraction
L	material characteristic length
L_{MD}	characteristic length of microstructural domain
m	Weibull modulus for crack initiation criterion
N	work-hardening exponent
P^{cr}_{frag}	critical probability for cracking of inclusions
v_0	reference volume for crack initiation criterion
V_f	inclusion volume fraction
α	inclusion aspect ratio $\alpha = a/b$
γ_0	viscosity constant
$\boldsymbol{\epsilon}$	microscopic strain tensor
ϵ_{fail}	strain to failure
θ	inclusion orientation
ι	cluster contour index
κ	cluster index
ν	Poisson's ratio
ρ	inclusion roundness $\rho = b/a$
$\boldsymbol{\sigma}$	microscopic stress tensor
σ_{max}	maximum tensile strength
σ_w	characteristic strength of inclusions
σ_y	initial yield stress of the underlying matrix without voids
σ_0	yield stress of the underlying matrix without voids
$\boldsymbol{\Sigma}$	macroscopic stress tensor

Abbreviations

Clus-1	single cluster hard core
Clus-3	triple cluster hard core
DOF	degree of freedom
DRA	discretely reinforced aluminum
GTN	Gurson–Tvergaard–Needleman
HC	hard core
LE-VCFEM	locally enhanced Voronoi cell finite element model
MAF	mean local area fraction
MNND	mean near neighbor distance
MPD	minimum permissible distance
MPD-CL	cluster minimum permissible distance
SDAF	standard deviation of local area fraction
SDNND	standard deviation of near neighbor distance
SEM	scanning electron microscopy
VCFEM	Voronoi cell finite element method
#CL	number of clusters
#INC	number of inclusions
#INC-CL	number of inclusions in cluster

over-simplification of the microstructure. Quite often, critical local features necessary to model strain to failure are lost in these models. Ductile fracture depends strongly on the extreme values of microstructural characteristics, e.g. nearest neighbor distances, highest local volume/area fraction, etc. and computational models must feature some of these characteristics for accuracy. Additionally, many of the existing studies have focused only on the initial stages of ductile damage, e.g. crack nucleation in the inclusions, and have not considered evolution of ductile failure by matrix void growth and coalescence.

Computational models developed by Ghosh et al. [26–32] have focused on more realistic representation of microstructures with non-uniform dispersion of heterogeneities. The microstructural Voronoi cell finite element model or VCFEM by Ghosh et. al. [26–31] offers significant promise for accurate micromechanical analysis of arbitrary heterogeneous microstructures with high efficiency. Morphological non-uniformities in dispersions, shapes and sizes, obtained from micrographs are readily modeled by this method [33]. This method has been extended in the locally enhanced VCFEM (LE-VCFEM) [32] to

model ductile fracture in heterogeneous microstructures. In LE-VCFEM, the stress-based hybrid VCFEM formulation is adaptively enhanced in regions of localized plastic flow to model stages of ductile fracture, from inclusion fragmentation to matrix cracking in the form of void nucleation, growth and coalescence. These regions are overlaid with finite deformation, displacement-based elements to accommodate strain softening in the constitutive behavior. LE-VCFEM has been demonstrated to be quite effective for simulating ductile fracture in [32].

This is the first of a two part paper on the effect of microstructural morphology and properties on ductile fracture in heterogeneous materials. In this part, extensive sensitivity studies are conducted with results of LE-VCFEM based micromechanical analyses of rate-dependent porous elastic–viscoplastic materials, to quantify the effects of loading rates, microstructural morphology and material properties on strain to failure. Based on the sensitivity study, a model is proposed for strain to failure, incorporating the effects of important morphological parameters. The 2D locally enhanced VCFEM is extended to rate-dependent porous elastic–viscoplastic materials in Section 2. In Section 3, sensitivity analyses with LE-VCFEM simulations are used to study the quantitative effect of applied strain rate, inclusion volume fraction, size, shape, orientation and spatial dispersion, as well as material properties on ductile fracture.

2. Locally enhanced VCFEM for ductile failure of heterogeneous rate-dependent ductile materials

In the locally enhanced Voronoi cell finite element model or LE-VCFEM [32], inclusions in a 2D microstructural section are assumed to be elastic and undergoing brittle fracture, while the matrix is represented by a pressure-dependent elasto-plastic model for porous materials undergoing ductile fracture. The assumed stress hybrid VCFEM formulation is modified in LE-VCFEM to admit local softening by the adaptive enrichment of critical regions of localized damage with displacement elements. Details of the LE-VCFEM formulation for ductile fracture of *rate-independent* microstructures are provided in [32]. In this paper, the LE-VCFEM formulation is extended to *rate-dependent* porous elastic–viscoplastic matrix materials. Rate-dependent models are important for modeling load conditions at elevated temperatures and high strain rates. The LE-VCFEM formulation for pressure-dependent elasto-viscoplastic porous material is discussed in this section.

Fig. 1a shows a multi-phase material microstructural section obtained from a scanning electron microscopy (SEM) of a cast aluminum alloy *W319* (Al–7%Si–3%Cu–0.4%Fe). The observed heterogeneities (in black) are silicon inclusions located at the boundary between two adjacent secondary aluminum dendrite arms. Fig. 1b shows the network of Voronoi cells

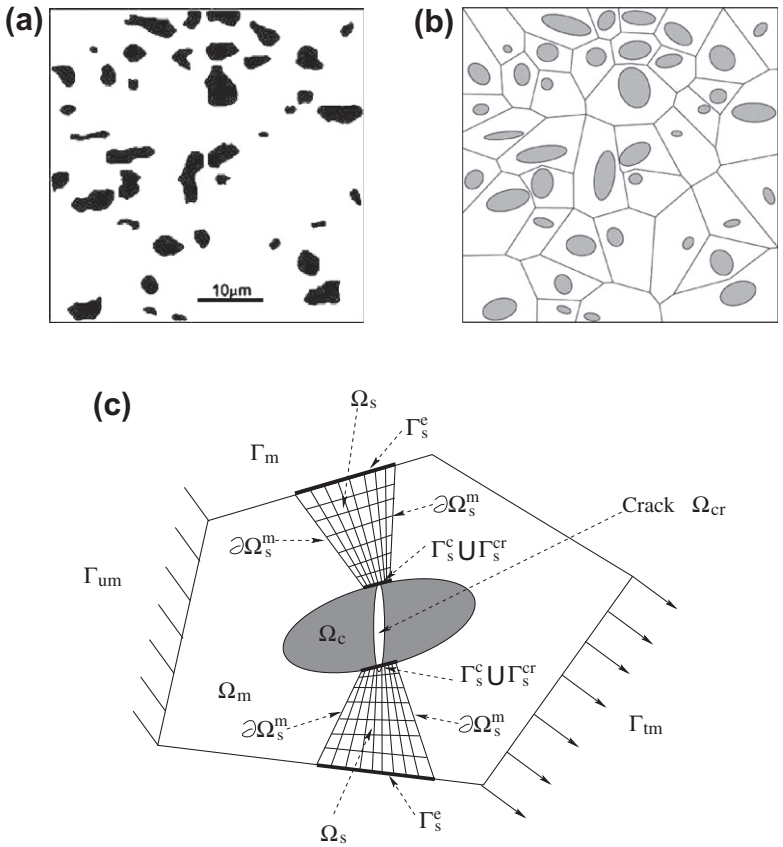

Fig. 1. (a) A micrograph of a cast aluminum alloy showing a distribution of Si inclusions, (b) VCFEM discretization, (c) a typical Voronoi cell element.

obtained by a tessellation process that takes into account the location, size and shape of inclusions [34]. Each cell represents the immediate neighborhood of an inclusion. The matrix and inclusion phases in each Voronoi cell are designated as Ω_m and Ω_c respectively as in Fig. 1c, while the inclusion crack phase is labeled as Ω_{cr}. Each Voronoi cell, containing the inclusion and crack phases in the matrix, is designated as an element in the Voronoi cell finite element (VCFE) formulation. Thus, $\Omega_e = \Omega_m \cup \Omega_c \cup \Omega_{cr}$. The element boundary $\partial\Omega_e$ is assumed to be comprised of a prescribed traction boundary Γ_{tm}, a prescribed displacement boundary Γ_{um}, and an inter-element boundary Γ_m, i.e. $\partial\Omega_e = \Gamma_{tm} \cup \Gamma_{um} \cup \Gamma_m$. The VCFEM formulation is based on an assumed stress hybrid formulation as detailed in [26].

In ductile fracture, inclusion cracking is followed by localization in ligaments of intense void evolution that results in a transition of the local stress–strain response from a strain hardening to a strain softening behavior. The assumed stress-based VCFEM formulation faces numerical instabilities associated with strain non-uniqueness in this regime. This can cause convergence problems, especially near the peak of the stress–strain curve, corresponding to the onset of softening. To avert instabilities, the stress-based VCFEM formulation *adaptively* incorporates a patch of high resolution displacement-based finite element in the strain softening region Ω_s of the matrix Ω_m in a Voronoi cell element [32]. This region is shown in Fig. 1c. Finite deformation porous elasto-viscoplasticity formulation governs the behavior of displacement-based elements in Ω_s. $\partial\Omega_s$ is the boundary of Ω_s and may consist of four distinct regions, depending on its overlap with pre-existing topological regions in the Voronoi cell element, i.e. $\partial\Omega_s = \Gamma_s^e \bigcup \Gamma_s^c \bigcup \Gamma_s^{cr} \bigcup \partial\Omega_s^m$. Here $\Gamma_s^e = \partial\Omega_e \cap \partial\Omega_s$, $\Gamma_s^c = \partial\Omega_c \cap \partial\Omega_s$ and $\Gamma_s^{cr} = \partial\Omega_{cr} \cap \partial\Omega_s$ represent the intersections of $\partial\Omega_s$ with the element, inclusion and crack boundaries respectively. The aggregate of these common boundaries is represented as $\Gamma_s = \Gamma_s^e \bigcup \Gamma_s^c \bigcup \Gamma_s^{cr}$.

Once the displacement-based local finite element region Ω_s is overlaid, a mapping procedure described in [35] is used to transfer local stresses, strains and material internal variables from the Voronoi cell element domain Ω_e to displacement elements in Ω_s. Superscript s labels variables associated with Ω_s. The mapping should guarantee displacement compatibility on the shared boundaries Γ_s between the stress and displacement interpolated regions as shown in Fig. 1c, i.e.

$$\mathbf{u}^s = \mathbf{u} \text{ on } \Gamma_s^e; \quad \mathbf{u}^s = \mathbf{u}' \text{ on } \Gamma_s^c; \quad \mathbf{u}^s = \mathbf{u}'' \text{ on } \Gamma_s^{cr} \tag{1}$$

Here $\mathbf{u}$, $\mathbf{u}'$ and $\mathbf{u}''$ are the displacements DOF's on the boundaries $\partial\Omega_e$, $\partial\Omega_c$ and $\partial\Omega_{cr}$ respectively.

2.1. Constitutive and damage relations for inclusion and matrix phases in each voronoi cell

2.1.1. Inclusion phase

The inclusion phase in each Voronoi cell element is assumed to be isotropic, linear elastic. Instantaneous cracking of an inclusion is assumed once a crack initiation criterion is satisfied at a point. A Weibull distribution based initiation criterion has been shown to represent experimental results accurately in [30,33]. In this criterion, a crack initiates when the probability function P_{frag} at any point in the inclusion exceeds a critical value. The probability function is defined as:

$$P_{frag}(v, \sigma_I^c) = 1 - exp\left[-\frac{v}{v_0}\left(\frac{\sigma_I^c}{\sigma_w}\right)^m\right] \tag{2}$$

where m and σ_w are the Weibull modulus and the characteristic strength respectively and v_0 is a reference volume that scales with the microstructure. The probability function incorporates the inclusion size v and the maximum principal stress σ_I^c in its interior. The introduction of inclusion size v in Eq. (2) follows experimental observations that larger inclusions have lower strengths due to a higher probability of having defects. The critical probability is taken to be $P_{frag}^{cr} = 95\%$. Once this criterion is met, a high aspect ratio elliptical crack is introduced at this point. An aspect ratio of $a/b = 10$ has been estimated to provide adequate resolution in representing inclusion splitting in [31]. Instantaneous inclusion splitting has been modeled in [30,33]. In this model, the ellipse extends slightly beyond the boundary of the inclusion from the point of initiation, manifesting complete inclusion splitting. The principal axis of this elliptical crack is normal to the direction of the maximum principal stress at the point.

2.1.2. Matrix phase

The matrix phase in each Voronoi cell element is modeled as a rate-dependent elastic–viscoplastic material containing microscopic voids. The corresponding matrix phase constitutive equations are developed as a rate-dependent viscoplasticity extension of the conventional rate-independent Gurson–Tvergaard–Needleman (GTN) model in [36–38]. In this constitutive model, the total strain rate is assumed to admit an additive decomposition into an elastic and viscoplastic part as:

$$\dot{\boldsymbol{\epsilon}} = \dot{\boldsymbol{\epsilon}}^{\mathbf{e}} + \dot{\boldsymbol{\epsilon}}^{\mathbf{p}} \tag{3}$$

For small elastic strains, the rate of Cauchy stress $\dot{\boldsymbol{\sigma}}$ is related to the elastic part of the strain rate tensor as: $\dot{\boldsymbol{\sigma}} = \mathbf{C}^{\mathbf{e}} : \dot{\boldsymbol{\epsilon}}^{\mathbf{e}}$, where $\mathbf{C}^{\mathbf{e}}$ is the fourth order isotropic elasticity tensor. The viscoplastic behavior of the porous ductile matrix is governed by the GTN yield function [39,40,37], given as:

$$\phi^{vp} = \left(\frac{q}{\bar{\sigma}_M}\right)^2 + 2f^* q_1 cosh\left(-\frac{3q_2 p}{2\bar{\sigma}_M}\right) - (1 + q_3 f^{*2}) = 0 \tag{4}$$

where $q = \sqrt{\frac{3}{2}\boldsymbol{\sigma}' : \boldsymbol{\sigma}'}$ and $p = -\frac{1}{3}\boldsymbol{\sigma} : \mathbf{I}$ are the Von-Mises equivalent stress and the hydrostatic pressure respectively, $\boldsymbol{\sigma}'$ is the deviatoric stress, f^* is a function of the void volume fraction f expressed in Eq. (20), and q_1, q_2, q_3 are void growth related parameters introduced in [40]. The denominator $\bar{\sigma}_M$ is the equivalent stress acting in the pure underlying matrix without voids. The subscript M is used to designate association with the pure underlying matrix without voids. Deformation in the matrix material is assumed to be governed by the viscoplastic over-stress model of Perzyna [41]. In this model, the viscoplastic strain rate is expressed in terms of a function $\Phi_M(F)$ of the over-stress F as (see [42]):

$$\dot{\boldsymbol{\epsilon}}^{\mathbf{p}}_M = \gamma_0 \langle \Phi_M(F) \rangle \frac{\partial \bar{\sigma}_M / \partial \boldsymbol{\sigma}_M}{\| \partial \bar{\sigma}_M / \partial \boldsymbol{\sigma}_M \|} \tag{5}$$

where γ_0 is a temperature dependent viscosity coefficient and $\langle\ \rangle$ is the MacCauley operator. A constant value $\gamma_0 = 10\ \mathrm{GPa}^{-1}\ \mathrm{s}^{-1}$ is used for the sensitivity study of this paper. The viscoplastic strain rate in Eq. (5) follows the associated flow rule and hence satisfies normality and incompressibility conditions. The over-stress F corresponds to the measure of excess loading stress over the rate-independent local yield strength σ_0 (an internal state variable), i.e.

$$F = \bar{\sigma}_M - \sigma_0(W_p) \tag{6}$$

Here W_p is the inelastic work and $\bar{\sigma}_M (= \sqrt{\frac{3}{2}\boldsymbol{\sigma}'_M : \boldsymbol{\sigma}'_M})$ in Eq. (4) is the effective matrix stress. The function $\Phi_M(F)$ may be chosen according to the material being modeled and the experimental conditions. In [41,42] a power law expression, i.e. $\Phi_M(F) = F^p$ has been discussed to adequately represent the behavior of most metals. The set of viscoplastic constitutive equations for the matrix material is complete with the evolution law of the yield strength σ_0. A linear hardening law, in which the rate of evolution of σ_0 linearly depends on the matrix equivalent plastic strain rate $\dot{\bar{\epsilon}}^p_M \left(= \sqrt{\frac{2}{3}\dot{\boldsymbol{\epsilon}}^p_M : \dot{\boldsymbol{\epsilon}}^p_M}\right)$, is assumed, i.e.:

$$\dot{\sigma}_0 = h(W_p)\dot{\bar{\epsilon}}^p_M \tag{7}$$

where $h(W_p)$ is the instantaneous plastic modulus. Using Eq. (5), the equivalent plastic strain rate $\dot{\bar{\epsilon}}^p_M$ can be expressed in terms of the over-stress function as:

$$\dot{\bar{\epsilon}}^p_M = \sqrt{\frac{2}{3}}\gamma_0 \langle \Phi_M(F) \rangle \tag{8}$$

Returning to the rate-dependent porous plasticity equations governing the porous matrix material behavior in each Voronoi cell element, the overall plastic strain rate is derived from the associated flow rule as:

$$\dot{\boldsymbol{\epsilon}}^{\mathbf{p}} = \dot{\lambda} \frac{\partial \phi^{vp}}{\partial \boldsymbol{\sigma}} \tag{9}$$

where $\dot{\lambda}$ is a viscoplastic multiplier that can be derived in terms of the matrix plastic strain rate $\dot{\boldsymbol{\epsilon}}^{\mathbf{p}}_M$. Assuming that the Hill-Mandel micro-macro energy condition [43] governs homogenization conditions for the porous matrix material, the rate of dissipative energy in the porous matrix material can be expressed as the product of the local equivalent stress $\bar{\sigma}_M$ and equivalent strain rate $\dot{\bar{\epsilon}}^p_M$ [44], i.e.

$$\boldsymbol{\sigma} : \dot{\boldsymbol{\epsilon}}^{\mathbf{p}} = \overline{\boldsymbol{\sigma}_M : \dot{\boldsymbol{\epsilon}}^{\mathbf{p}}_M} = (1-f)\bar{\sigma}_M \dot{\bar{\epsilon}}^p_M \tag{10}$$

The overbar in Eq. (10) corresponds to the ensemble average over a representative volume element. The viscoplastic multiplier $\dot{\lambda}$ may then be obtained by substituting the flow rule (9) into the energy Eq. (10) as:

$$\dot{\lambda} = (1-f)\sqrt{\frac{2}{3}} \frac{\bar{\sigma}_M}{\boldsymbol{\sigma} : \frac{\partial \phi^{vp}}{\partial \boldsymbol{\sigma}}} \gamma_0 \langle \Phi_M(F) \rangle \tag{11}$$

The resulting flow rule is stated as:

$$\dot{\boldsymbol{\epsilon}}^{\mathbf{p}} = (1-f)\sqrt{\frac{2}{3}} \frac{\bar{\sigma}_M}{\boldsymbol{\sigma} : \frac{\partial \phi^{vp}}{\partial \boldsymbol{\sigma}}} \gamma_0 \langle \Phi_M(F) \rangle \frac{\partial \phi^{vp}}{\partial \boldsymbol{\sigma}} \tag{12}$$

The rate of evolution of the local macroscopic void volume fraction f is divided into growth and nucleation parts, as discussed in [36–38], as:

$$\dot{f} = \dot{f}_{growth} + \dot{f}_{nucleation} \tag{13}$$

The matrix void growth rate due to the dilatation is written as:

$$\dot{f}_{growth} = (1-f)\dot{\epsilon}^p_{kk} \tag{14}$$

This expression accounts for plastic incompressibility in the underlying matrix. The rate of plastic strain controlled void nucleation is expressed in terms of the effective plastic strain $\bar{\epsilon}^p_M$ in the underlying matrix [36] as:

$$\dot{f}_{nucleation} = A(\bar{\epsilon}^p_M)\dot{\bar{\epsilon}}^p_M \tag{15}$$

where

$$A(\bar{\epsilon}_M^p) = \frac{f_N}{s_N\sqrt{2\pi}} \exp\left[-\frac{1}{2}\left(\frac{\bar{\epsilon}_M^p - \epsilon_N}{s_N}\right)^2\right] \tag{16}$$

Here ϵ_N is the mean nucleation strain, s_N is its standard deviation, and f_N is the intensity of void nucleation.

The rate-dependent porous plasticity model does not incorporate a material length scale, and hence numerical simulations of ductile fracture exhibit mesh sensitivity. To avoid this pathological shortcoming, a non-local evolution equation for the void volume fraction has been proposed in [38]. In this formulation, the non-local growth rate of the void volume fraction at a material point $\bar{\mathbf{x}}$ is given as:

$$\dot{f}^{non\text{-}local} = \frac{1}{W(\bar{\mathbf{x}})}\int_{\Omega_m} \dot{f}(\mathbf{x}) w(|\mathbf{x}-\bar{\mathbf{x}}|)\mathrm{d}\Omega \tag{17}$$

where

$$W(\bar{\mathbf{x}}) = \int_{\Omega_m} w(|\mathbf{x}-\bar{\mathbf{x}}|)\mathrm{d}\Omega \quad \text{and} \quad w(|\mathbf{x}|) = \left[\frac{1}{1+(|\mathbf{x}|/L)^p}\right]^q \tag{18}$$

Here $p = 8$, $q = 2$ and $L > 0$ is a material characteristic length, which regularizes the localization problem. The weighting function $w(|\mathbf{x}|) = 1$ at $|\mathbf{x}| = 0$, $w(|\mathbf{x}|) = 0.25$ at $|\mathbf{x}| = L$ and $w(|\mathbf{x}|) \to 0 \forall |\mathbf{x}| > L$ with a narrow transition region. Non-locality is associated with spatial gradients of $\dot{f}$. Evolution of the local void volume fraction f is expressed in terms of its non-local rate $\dot{f}^{non\text{-}local}$ as:

$$f \triangleq f_0 + \int df^{non\text{-}local} \tag{19}$$

where f_0 is the inital void volume fraction in the matrix.

Finally, an acceleration function f^* is introduced in Eq. (4) to model the complete loss of material stress carrying capacity due to void coalescence [37] as:

$$f^* = \begin{cases} f & f \leqslant f_c \\ f_c + \frac{f_u^* - f_c}{f_f - f_c}(f - f_c) & f > f_c \end{cases} \tag{20}$$

f_c is the critical void volume fraction at which void coalescence first occurs and f_f is the value at final failure. As the void volume fraction $f \to f_f$, the acceleration function $f^* \to f_u^* = 1/q_1$. At this value, the yield surface shrinks to a point manifesting loss of material load capacity. To avoid numerical difficulties, $f \to 0.95 f_f$ is used in Eq. (20). The value of f is frozen once it reaches $0.95 f_f$ at an element quadrature point, implying local ductile material failure.

2.1.3. Finite deformation constitutive relations for the enhanced region Ω_s

Finite deformation kinematics and constitutive laws are considered for the locally enhanced matrix region $\Omega_s \in \Omega_m$ in a Voronoi cell element undergoing strain localization (see Fig. 1). The finite deformation formulation of the rate-dependent porous plasticity constitutive relations follows a framework developed in [42]. In this formulation, the constitutive relations are written in a rotated Lagrangian system in terms of the rotated Cauchy stress tensor $\boldsymbol{\sigma}_R^s = \mathbf{R}^T\boldsymbol{\sigma}^s\mathbf{R}$ and the rotated rate of deformation tensor $\mathbf{D}_R^s = \mathbf{R}^T\mathbf{D}^s\mathbf{R}$, as described in [45]. Here $\mathbf{R}$ is a proper orthogonal tensor representing a pure rotation obtained from the polar $\mathbf{RU}$ decomposition of the deformation gradient tensor $\mathbf{F}^s = \nabla_0\mathbf{x}^s$, where the subscript 0 refers to the reference configuration.

2.2. Time integration schemes for strain and stress updates in the voronoi cell element

Voronoi cell element partitioning into subregions Ω_s and $\Omega_{m'} = \Omega_m \setminus \Omega_s$ requires different integration schemes for the rate-dependent plasticity constitutive relations in the two subregions. In the stress interpolated region of the matrix $\Omega_{m'} = \Omega_m \setminus \Omega_s$, an implicit strain update algorithm is implemented using the Newton–Raphson method. In the enhanced subdomain Ω_s with displacement interpolated elements, a stress update algorithm is used. These algorithms are briefly discussed next.

2.2.1. Strain update algorithm for the stress interpolated subdomain $\Omega_{m'}$

An implicit strain update algorithm is developed for $\Omega_{m'}$ using the unconditionally stable backward Euler algorithm. The incremental update method considers small strain kinematics for the generalized plane strain condition. With prescribed in-plane stress increments $\Delta\sigma_{ij}$, $(i,j = 1,2)$ and incremental out-of-plane strain $\Delta\epsilon_{33}$, the algorithm computes increments in the total strain $\Delta\epsilon_{ij}$, $(i,j = 1,2)$, plastic strain $\Delta\epsilon_{ij}^p$, $(i,j = 1,2,3)$, out-of-plane stress $\Delta\sigma_{33}$, as well as the state variables f, σ_0, and $\bar{\epsilon}_M^p$. By expressing the constitutive relations in terms of the hydrostatic stress p and the equivalent stress q, the strain update algorithm can be reduced to a three-parameter nonlinear problem. The corresponding three nonlinear equations, used to

solve the system are derived from the flow rule, the viscoplastic law and the generalized plane strain condition as enumerated below.

(1) Rate-dependent flow rule: Eq. (9) can be divided into hydrostatic and deviatoric parts as:

$$\dot{\boldsymbol{\epsilon}}^{\mathbf{p}} = \dot{\lambda}\frac{\partial \phi^{vp}}{\partial \boldsymbol{\sigma}} = \dot{\lambda}\left(-\frac{1}{3}\frac{\partial \phi^{vp}}{\partial p}\mathbf{I} + \frac{\partial \phi^{vp}}{\partial q}\mathbf{n}\right) \tag{21}$$

where $\mathbf{n} = \frac{3}{2q}\boldsymbol{\sigma}'$ is a unit normal tensor representing the flow direction of the deviatoric plastic strain, and the stress is decomposed into hydrostatic and deviatoric parts as $\boldsymbol{\sigma} = -p\mathbf{I} + \frac{2}{3}q\mathbf{n}$. The strain rate in Eq. (21) is integrated in the time step Δt between t^n and t^{n+1} by the backward Euler algorithm, as:

$$\Delta\boldsymbol{\epsilon}^{\mathbf{p}} = \frac{1}{3}\Delta\epsilon_p\mathbf{I} + \Delta\epsilon_q\mathbf{n}^{n+1} \tag{22}$$

All quantities in the backward Euler algorithm are evaluated at the end of the increment at t^{n+1}, yielding:

$$\Delta\epsilon_p = -\Delta\lambda\left(\frac{\partial \phi^{vp}}{\partial p}\right)^{n+1} \quad \text{and} \quad \Delta\epsilon_q = \Delta\lambda\left(\frac{\partial \phi^{vp}}{\partial q}\right)^{n+1} \tag{23}$$

Eliminating $\Delta\lambda$ from the two expressions in Eq. (23) leads to:

$$\Delta\epsilon_p\left(\frac{\partial \phi^{vp}}{\partial q}\right)^{n+1} + \Delta\epsilon_q\left(\frac{\partial \phi^{vp}}{\partial p}\right)^{n+1} = 0 \tag{24}$$

(2) Viscoplastic law: Integrating Eq. (11) for the increment of viscoplastic multiplier, i.e. $\Delta\lambda = \Delta t\dot{\lambda}^{n+1}$, and incorporating the second relation in (23) results in:

$$\Delta\epsilon_q - \Delta\lambda\left(\frac{\partial \phi^{vp}}{\partial q}\right)^{n+1} = 0 \tag{25}$$

(3) Generalized plane strain condition: This condition is expressed with a specified out-of-plane normal strain increment, i.e. $\Delta\epsilon_{33} = \Delta\epsilon^e_{33} + \Delta\epsilon^p_{33} = \hat{\epsilon}^{constant}$. Substituting the expression for $\Delta\epsilon^e_{33}$ from the generalized Hooke's law into the plane strain condition and using Eq. (22), yields (see [32]):

$$\frac{1}{E}(\Delta\sigma_{33} - \nu\Delta\sigma_{11} - \nu\Delta\sigma_{22}) + \Delta\lambda\left(-\frac{1}{3}\frac{\partial \phi^{vp}}{\partial p} + \frac{3\sigma'_{33}}{2q}\frac{\partial \phi^{vp}}{\partial q}\right)^{n+1} - \hat{\epsilon}^{constant} = 0 \tag{26}$$

where ν and E are the Poisson's ratio and Young's modulus respectively. The expressions of $\Delta\epsilon_p$ or $\Delta\epsilon_q$ in Eq. (23) may be used to eliminate the plastic multiplier $\Delta\lambda$.

At each integration point in $\Omega_{m'}$, Eqs. (24)–(26) are iteratively solved for $\Delta\epsilon_p$, $\Delta\epsilon_q$, and $\Delta\sigma_{33}$ using the Newton–Raphson method. Specifically three nonlinear algebraic equations

$$A_{i1}c_p + A_{i2}c_q + A_{i3}c_\sigma = b_i \quad i = 1,2,3 \tag{27}$$

are solved for the iterative correction parameters c_p, c_q and c_σ to the solution variables $\Delta\epsilon_p$, $\Delta\epsilon_q$ and $\Delta\sigma_{33}$. The coefficients A_{ij} and b_i are given in Appendix A. The state variables are then updated using the evolution equations:

$$\Delta f = (1-f)\Delta\epsilon_p + A\Delta\bar{\epsilon}^p_M, \quad \Delta\sigma_0(W_p) = h(W_p)\Delta\bar{\epsilon}^p_M \tag{28}$$

where the increment of equivalent matrix plastic strain is expressed as:

$$\Delta\bar{\epsilon}^p_M = \frac{-p\Delta\epsilon_p + q\Delta\epsilon_q}{(1-f)\bar{\sigma}_M} \tag{29}$$

Finally, the increment of the total strain tensor is computed as $\Delta\boldsymbol{\epsilon} = \Delta\boldsymbol{\epsilon}^{\mathbf{e}} + \Delta\boldsymbol{\epsilon}^{\mathbf{p}}$. The increment $\Delta\boldsymbol{\epsilon}^{\mathbf{e}}$ is obtained from elasticity relations at t^{n+1} and $\Delta\boldsymbol{\epsilon}^{\mathbf{p}}$ is calculated from Eq. (22).

2.2.2. Stress update algorithm for the displacement interpolated subdomain Ω_s

Finite deformation rate-dependent porous plasticity constitutive relations in Ω_s are integrated by a rate-dependent finite deformation extension of the backward Euler algorithm proposed in [46]. The rotated Cauchy stress is updated in the increment Δt between configurations Ω^n_s and Ω^{n+1}_s as:

$$\begin{aligned}\left(\boldsymbol{\sigma}_R^s\right)^{n+1} &= \left(\boldsymbol{\sigma}_R^s\right)^n + \Delta\boldsymbol{\sigma}_R^s = \left(\boldsymbol{\sigma}_R^s\right)^n + \mathbf{C}^{\mathbf{e}} : \Delta\boldsymbol{\epsilon}_R^{\mathbf{se}} \\ &= \left(\boldsymbol{\sigma}_R^s\right)^n + \mathbf{C}^{\mathbf{e}} : \left(\Delta\boldsymbol{\epsilon}_R^s - \Delta\boldsymbol{\epsilon}_R^{\mathbf{sp}}\right) \\ &= \boldsymbol{\sigma}_R^{\mathbf{se}} - \mathbf{C}^{\mathbf{e}} : \Delta\boldsymbol{\epsilon}_R^{\mathbf{sp}}\end{aligned} \tag{30}$$

The superscript s is associated with the subdomain Ω_s. The elastic predictor for this integration algorithm is defined as:

$$\boldsymbol{\sigma}_R^{\mathbf{se}} = \left(\boldsymbol{\sigma}_R^s\right)^n + \mathbf{C}^{\mathbf{e}} : \Delta\boldsymbol{\epsilon}_R^s \tag{31}$$

Here $\Delta\boldsymbol{\epsilon}_R^{\mathbf{se}} = \Delta t\left(\mathbf{D}_R^{\mathbf{se}}\right)^{n+1}$ and $\Delta\boldsymbol{\epsilon}_R^{\mathbf{sp}} = \Delta t\left(\mathbf{D}_R^{\mathbf{sp}}\right)^{n+1}$ are increments of the rotated elastic and plastic strain tensors respectively. The rotated stress increment $\Delta\boldsymbol{\sigma}_R^s$ is calculated using an update algorithm, corresponding to a known increment in the strain tensor $\Delta\boldsymbol{\epsilon}^s$, which is related to the rotated strain increment as:

$$\begin{aligned}\Delta\boldsymbol{\epsilon}_R^s &= (\mathbf{R}^T)^{n+1}\Delta\boldsymbol{\epsilon}^s\mathbf{R}^{n+1} \\ &= (\mathbf{R}^T)^{n+1}\frac{1}{2}\left\{\left(\frac{\partial\Delta\mathbf{u}^s}{\partial\mathbf{x}}\right) + \left(\frac{\partial\Delta\mathbf{u}^s}{\partial\mathbf{x}}\right)^T\right\}\mathbf{R}^{n+1}\end{aligned} \tag{32}$$

$\Delta\mathbf{u}^s$ corresponds to the displacement increment in the interval. The stress increment is obtained by solving the nonlinear constitutive relations of Section 2.1.2 in the rotated Lagrangian coordinates.

With known in-plane strain increments $\Delta\epsilon_{ij}^s, (i,j=1,2)$ and the incremental out-of-plane strain $\Delta\epsilon_{33}^s$, the following variables are evaluated in the time increment $t^{n+1} - t^n$.

(1) Increments of in-plane stress components $\Delta\sigma_{ij}^s,\ i,j=1,2$.
(2) Increments of out-of-plane stress $\Delta\sigma_{33}^s$.
(3) Increments of plastic strain tensor $\Delta\epsilon_{ij}^{\mathbf{sp}}$.
(4) Internal variables f, σ_0 and $\bar{\epsilon}_M^p$.

The dependence of the constitutive relations on the stress tensor can be reduced to dependence on the hydrostatic pressure p_R^s and equivalent stress q_R^s in the rotated Lagrangian system. Consequently, the stress update algorithm can be reduced to a two-parameter nonlinear problem involving the hydrostatic and deviatoric parts of the constitutive relations. The generalized plane strain condition need not be added as a third equation, since it is automatically enforced as $\Delta\epsilon_{33}^s = \hat{\epsilon}^{constant}$.

The rotated Cauchy stress $\left(\boldsymbol{\sigma}_R^s\right)^{n+1}$ is related to hydrostatic and deviatoric components of the incremental rotated plastic strain $\Delta\epsilon_{Rp}$ and $\Delta\epsilon_{Rq}$ by substituting Eq. (22) in Eq. (30) and expressing the elasticity tensor in terms of the shear and bulk moduli as $C_{ijkl}^e = 2G\delta_{ik}\delta_{jl} + \left(K - \frac{2}{3}G\right)\delta_{ij}\delta_{kl}$. This yields:

$$\left(\boldsymbol{\sigma}_R^s\right)^{n+1} = \boldsymbol{\sigma}_R^{\mathbf{se}} - K\Delta\epsilon_{Rp}\mathbf{I} - 2G\Delta\epsilon_{Rq}\left(\mathbf{n}_R^s\right)^{n+1} \tag{33}$$

The deviatoric part of the stress update is along $\left(\mathbf{n}_R^s\right)^{n+1}$, which implies that $\left(\boldsymbol{\sigma}_R^{\mathbf{se}}\right)'$ and the deviatoric part of $\left(\boldsymbol{\sigma}_R^s\right)^{n+1}$ are coaxial and therefore $\left(\mathbf{n}_R^s\right)^{n+1}$ can be computed from the elastic predictor $\boldsymbol{\sigma}_R^{\mathbf{se}}$ [46] as:

$$\left(\mathbf{n}_R^s\right)^{n+1} = \frac{3}{2q_R^{se}}\left(\boldsymbol{\sigma}_R^{\mathbf{se}}\right)' \tag{34}$$

The two nonlinear equations to be solved for $\Delta\epsilon_{Rp}$ and $\Delta\epsilon_{Rq}$ are then derived from the flow rule and the viscoplastic law in the rotated Lagrangian frame, as discussed in Section 2.2.1.

(1) Rate-dependent flow rule:

$$\Delta\epsilon_{Rp}\left(\frac{\partial\phi^{vp}}{\partial q^s}\right)_R^{n+1} + \Delta\epsilon_{Rq}\left(\frac{\partial\phi^{vp}}{\partial p^s}\right)_R^{n+1} = 0 \tag{35}$$

(2) Viscoplastic law:

$$\Delta\epsilon_{Rq} - \Delta\lambda\left(\frac{\partial\phi^{vp}}{\partial q^s}\right)_R^{n+1} = 0 \tag{36}$$

Eqs. (35) and (36) are solved in conjunction with the evolution laws (28) and (29) using the Newton–Raphson iteration method. Corrections c_p and c_q to the primary solution variables $\Delta\epsilon_{Rp}$ and $\Delta\ \epsilon_{Rq}$ are solved from the equations

$$A_{i1}c_p + A_{i2}c_q = b_i \quad i=1,2 \tag{37}$$

The coefficients A_{ij} and b_i are given in Appendix B. The rotated Cauchy stress $\left(\boldsymbol{\sigma}_R^s\right)^{n+1}$ is then calculated from Eq. (33). The state variables $\bar{\epsilon}_M^p, f$, and σ_0 are updated using relations (28) and (29) and the rotated plastic strain tensor $\left(\boldsymbol{\epsilon}_R^{\mathbf{sp}}\right)^{n+1}$ is obtained from Eq. (22) as:

$$\left(\boldsymbol{\epsilon}_R^{\mathbf{sp}}\right)^{n+1} = \left(\boldsymbol{\epsilon}_R^{\mathbf{sp}}\right)^{n} + \left(\frac{1}{3}\Delta\epsilon_{Rp}\mathbf{I} + \Delta\epsilon_{Rq}\left(\mathbf{n}_R^s\right)^{n+1}\right) \tag{38}$$

Subsequently, the stress $(\boldsymbol{\sigma}^s)^{n+1}$, plastic strain $(\boldsymbol{\epsilon}^{\mathbf{sp}})^{n+1}$ and corresponding increments in Ω_s^{n+1} are obtained by tensor rotation.

3. Sensitivity of ductile fracture with LE-VCFEM analysis of simulated microstructures

Sensitivity of ductile failure to loading rates, microstructural morphology and material properties are examined with the rate-dependent LE-VCFEM model discussed in Section 2.

3.1. Effect of the applied strain rate

The LE-VCFEM model is implemented to study the sensitivity of ductile fracture on applied strain rate for a uniform microstructural unit cell of an aluminum silicon carbide metal–matrix composite. Three uniaxial tensile strain rate conditions are applied to the unit cell under plane strain in the horizontal (x) direction. They are: (i) $\dot{e}_{xx}^{(1)} = 1.0 \times 10^{-3}\ \mathrm{s}^{-1}$, (ii) $\dot{e}_{xx}^{(2)} = 1.0 \times 10^{-1}\ \mathrm{s}^{-1}$, and (iii) $\dot{e}_{xx}^{(3)} = 2.0 \times 10^{-1}\ \mathrm{s}^{-1}$. For a total prescribed displacement $\Delta u = 0.1$, these correspond to time intervals, $\Delta t = 100$ s, 1 s, and 0.5 s respectively. The microstructure is unconstrained in the vertical (y) direction. For comparison, the rate-independent response corresponding to $\gamma_0 \to \infty$ is also examined.

The microstructural domain is a square (1×1) unit cell as shown in the inset of Fig. 2. It consists of a single circular silicon carbide (SiC) inclusion of area fraction $V_f = 20\%$. Material and inclusion cracking properties of SiC have been calibrated in [33] and values used in simulations are given in Table 1. The reference volume fraction v_0 in the Weibull model for the single inclusion case is assumed to be equal to the inclusion volume fraction of the unit cell.

The matrix hardening behavior is represented by a power law model,

$$\sigma_0 = \sigma_y\left(\frac{\bar{\epsilon}_M^p}{\epsilon_y} + 1\right)^N \tag{39}$$

where σ_y is the yield stress, N is the hardening exponent and $\epsilon_y = \sigma_y/E$ is the elastic strain at onset of yielding. Constitutive parameters in Section 2.1.2 for the Al alloy matrix are delineated in Table 2. The initial porosity content of the matrix f_0 is

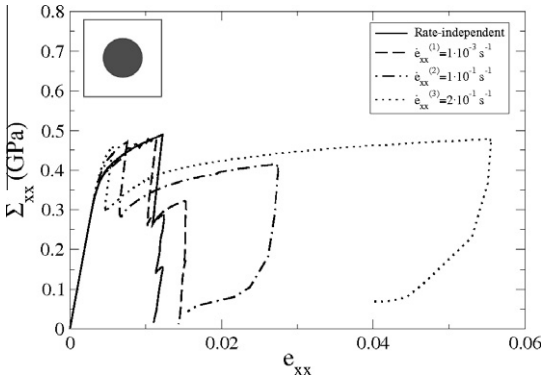

Fig. 2. Averaged macroscopic stress–strain response for a unit cell with a single circular inclusion at different uniaxial tensile strain rates.

Table 1
Elastic and inclusion cracking properties in Eq. (2) for SiC inclusions.

Cases	E (GPa)	v	σ_w (MPa)	m	v_0	P_{frag}^{cr} (%)
Single inclusion	427	0.17	400	2.4	0.2	95
Multiple inclusions	427	0.17	500	2.4	0.004	95

Table 2
Elastic, plastic and void evolution properties for the Al alloy matrix.

E (GPa)	v	σ_y (MPa)	N	γ_0 (GPa^{-1} s^{-1})	p	f_0	f_c	f_f
72	0.32	340	0.135	10	1	0.001	0.15	0.25

assumed to be 0.1% and the void evolution related constants are set to $q_1 = 1.5$, $q_2 = 1$, $q_3 = 2.25$. The void nucleation parameters in Eq. (16) are $\epsilon_N = 0.3$, $s_N = 0.1$ and $f_N = 0.04$. In classical homogenization theories, the size of the microstructural domain is immaterial and does not affect the solution. The use of a non-local evolution law for void volume fraction f in Eq. (19) introduces a length scale L to the problem and hence, the size of the microstructural region affects the solution. For the one inclusion microstructural domain of size 1×1, the authors have determined from numerical experiments that a value $L = 0.1$ regularizes the solution adequately.

Fig. 2 shows the averaged stress–strain response for different loading rates. The first sharp stress drop corresponds to inclusion cracking, while the final drop signals complete ductile failure of the microstructural domain. Strain rate is found to play an important role on the ductile fracture of rate-sensitive heterogeneous materials. For rate-dependent materials, higher applied strain rates lead to increased elastic straining and reduced plastic deformation of the matrix. This in turn, induces higher stresses in both the matrix and inclusion phases. For a given applied macroscopic strain, the stress in the inclusion is much higher for larger strain rates, as illustrated in the stress contour plots of Fig. 3. The figures show stress contours for (i) a rate-independent material and (ii) a rate-dependent material with an applied strain rate of $\dot{e}^{(3)}_{xx} = 2.0 \times 10^{-1}\ s^{-1}$, corresponding to a strain of 5.56×10^{-3} at which the inclusion cracks in the rate-dependent material. The stress level and its spread, especially in the inclusion, are significantly different for the two cases. This causes inclusion cracking at a lower applied strain for the rate-dependent material. Despite this early inclusion cracking, the neighboring matrix undergoes limited plastic deformation at higher strain rates. This results in a smaller evolution rate of porosities, even near the crack tip. Strain to failure is thus enhanced at higher strain rates due to the delay of plastic response in the matrix. Similar observations have been made in [47] for a silicon carbide reinforced aluminum metal matrix composite at high temperatures. While higher loading rates are found to improve ductility of the one inclusion microstructural domain depicted in the inset of Fig. 2, it is prudent to assume that such inferences cannot be generalized for more complex microstructures or for different material properties. In these cases, early cracking can have different effects on the overall ductile cracking behavior. Ductility at high loading rates entails a competition between early inclusion cracking and reduced void nucleation and growth in vicinity of crack tips.

3.2. Effect of microstructural morphology on ductility

The dependence of ductility or strain to failure on spatial distribution, size, shape and volume fraction of inclusions in the microstructure are investigated in this section. Experimental studies in [11–14] have demonstrated that damage in heterogeneous ductile materials initiates in regions of high clustering by cracking of larger and elongated inclusions. Computer simulated microstructures are analyzed by LE-VCFEM with special focus on the effects of clustering and inclusion geometry. Micromechanical LE-VCFEM analyses of the microstructural domains are conducted for rate-independent case under plane strain conditions. The incremental out-of-plane strain is set to $\Delta\epsilon_{33} = 0$ for these simulations. Material properties are the same as in Section 3.1 except for the inclusion cracking parameters. The Weibull parameters are $\sigma_w = 500$ MPa, $m = 2.4$, $v_0 = 0.004$, and $P^{cr}_{frag} = 95\%$. The material characteristic length (MCL) is set to $L = 0.014$.

3.2.1. Microstructural simulation and quantitative characterization

Five computer simulated microstructural domains are generated as shown in Fig. 4. Each microstructural domain is a unit (1×1) square domain containing 25 inclusions with an overall inclusion volume fraction of 10%. The microstructural domains (a) to (c) contain 25 circular elastic inclusions of same size, that are dispersed in different spatial distributions. Specifically, three different patterns are considered:

- *Hard core (HC)*: This is a variant of a pure random Poisson pattern with two imposed constraints [48], viz.: (a) no two inclusions are allowed to overlap and (b) all inclusions are completely contained within the region. The minimum permissible distance (MPD) between inclusion surfaces or between an inclusion and a boundary are prescribed.

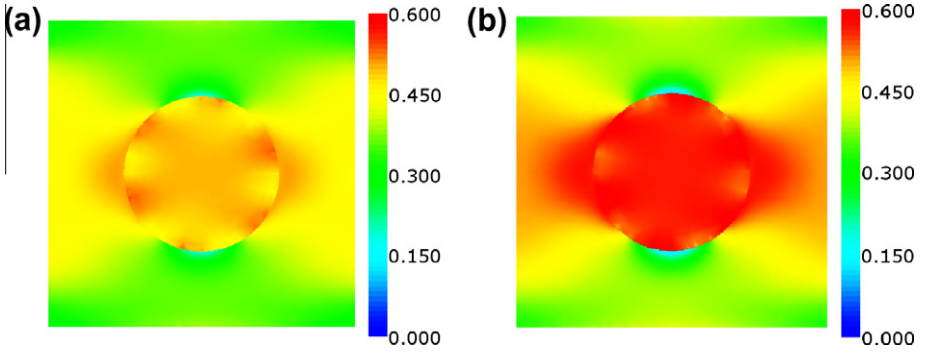

Fig. 3. Stress contours of σ_{xx} (in GPa) at a macroscopic strain $e_{xx} = 5.56 \times 10^{-3}$ for (a) rate-independent material, and (b) rate-dependent material at $\dot{e}^{(3)}_{xx} = 2.0 \times 10^{-1}\ s^{-1}$.

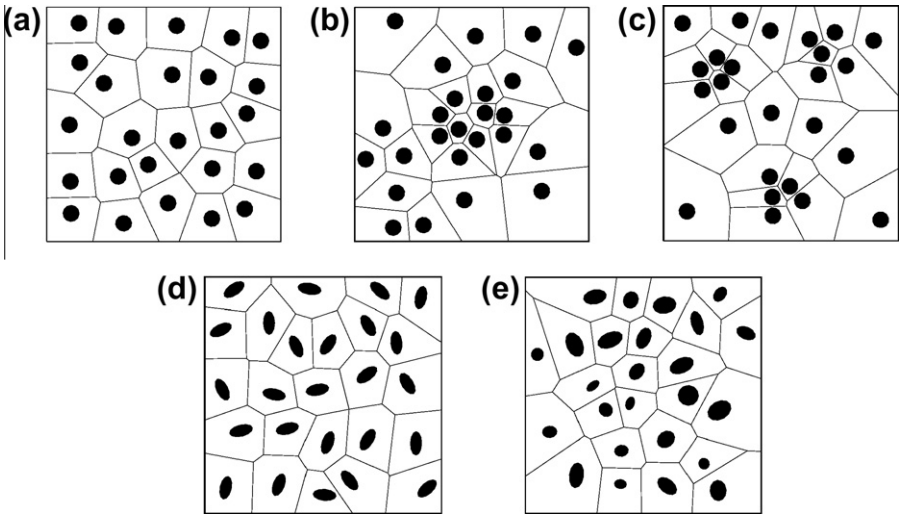

Fig. 4. Computer generated microstructures of volume fraction 10% containing 25 inclusions with the following characteristics: (a) circular inclusions in hard core dispersion, (b) circular inclusions with one cluster, (c) circular inclusions with three clusters, (d) identical elliptical inclusions of random orientation in HC dispersion, (e) elliptical inclusions of random shape and orientation in HC dispersion.

- *Single cluster hard core model (Clus-1)*: This is characterized by a decreased average inclusion MPD within a subregion of the otherwise hard core microstructural domain.
- *Triple cluster hard core model (Clus-3)*: This is characterized by a decreased average inclusion MPD, within three subregions of an otherwise hard core microstructural domain.

Microstructures in Fig. 4a–c are intended to investigate the effect of inclusion clustering on ductility. Microstructures (d) and (e) contain 25 elliptical inclusions of different sizes, shapes and orientations in hard core dispersions. They are created to study the influence of inclusion geometry.

Characteristic parameters used for generating the five microstructural domains are listed in Table 3. The inclusion major and minor axes a and b are determined from the inclusion volume fraction (V_f), aspect ratio $\alpha = \frac{a}{b}$ and number of inclusions (#INC). A random generator is used to disperse the inclusions with predetermined parameters, viz. number of clusters (#CL), minimum permissible distance within the cluster (MPD-CL) and outside (MPD), and the number of inclusions within each cluster (#INC-CL).

The microstructural domains are tessellated into Voronoi cell meshes using a 2D mesh generator developed in [34]. Each Voronoi cell represents the neighborhood of an embedded inclusion. Consequently it can be used to calculate the local area fraction, near neighbor and nearest neighbor distances and other descriptors of microstructural morphology. The microstructural morphology can be quantitatively characterized using different statistical functions of shape, size and distribution [48–51]. Table 4 lists some characterization parameters for the microstructures in Fig. 4. For each simulated microstructure, the statistical mean and standard deviation of the local area fraction (MAF and SDAF) and near neighbor distances (MNND and SDNND) respectively are computed. The local area fraction is measured as the ratio of inclusion area to that of the associated Voronoi cell. MAF for all microstructures is larger than the overall area fraction, as was noted in [48]. Higher values of MAF and SDAF are associated with the clustered patterns. This manifests a larger area fraction of inclusions inside the clusters. Near neighbor distances are determined as the surface to surface distance between inclusions that share a common Voronoi cell edge. MNND decreases with higher clustering manifesting stronger interaction between inclusions. Concurrently, SDNND increases due to variation of near neighbor distances throughout the microstructure.

The last two columns are additional metrics developed in [52] for quantifying the level of clustering. The cluster index κ quantifies the number of inclusions in a particular region and the area of matrix that is free of inclusions. While κ takes higher

Table 3
Parameters used for the generation of the microstructural domains of Fig. 4.

Cases	V_f (%)	#CL	#INC	a	b	MPD	#INC-CL	MPD-CL
(a)	10	0	25	0.0714	0.0714	0.05	–	–
(b)	10	1	25	0.0714	0.0714	0.05	11	0.005
(c)	10	3	25	0.0714	0.0714	0.05	5	0.005
(d)	10	0	25	0.1010	0.0505	0.05	–	–
(e)	10	0	25	–	–	0.05	–	–

Table 4
Statistics characterizing microstructural morphology of computer simulated microstructural domains of Fig. 4.

Cases	MAF	SDAF	MNND	SDNND	κ	ι
(a)	0.1030	0.0184	0.0820	0.0282	4.18	0.632
(b)	0.1478	0.0973	0.0641	0.0490	8.25	0.771
(c)	0.1332	0.0792	0.0631	0.0764	6.01	0.800
(d)	0.1028	0.0177	0.0945	0.0292	4.12	0.505
(e)	0.1068	0.0465	0.0799	0.0289	4.36	0.690

values for highly clustered microstructures, it is not bounded. The cluster contour index $\iota \in [0,1]$ is a measure of the area fraction of inclusions in the cluster, and is more relevant for microstructures with variable inclusion sizes. Its value varies from 0 for a uniform microstructure to 1 for a high level of clustering.

3.2.2. Sensitivity to clustering

To study the inter-dependence between ductility and clustering, LE-VCFEM simulations of the microstructural domains in Fig. 4a–c are conducted with an applied tensile strain in the horizontal (x) direction. For microstructures (a) and (b), the corresponding averaged (macroscopic) stress–strain response is plotted in Fig. 5. Contour plots of the final void volume fraction with clear delineation of the ductile fracture path are also shown for microstructures (a) and (b) in the Fig. 6. The numbers on the damaged inclusions in Fig. 6 indicate the cracking sequence in the simulation. The microstructural domain with HC distribution results in much higher ductility than those with the 1-Cluster or 3-Cluster distributions. While a higher level of clustering results in increased inclusions cracking within the clusters, it is not necessary that these would propagate significant amount of void growth in the matrix.

The dependence of strain to failure on clustering is quantified in Table 5, where the cluster index κ and cluster contour index ι are tabulated against the maximum tensile strength σ_{max} and the strain to failure ϵ_{fail}. The strain to failure ϵ_{fail} is obtained by extending the drop in the stress–strain plots (softening portion) of Fig. 5 to intercept the x-axis. Microstructural domains characterized by lower values of κ and ι, have higher ductility and also higher maximum stress. The cluster contour index ι is found to have a better correlation with ϵ_{fail}, meaning that inclusion volume fraction within the cluster is a better

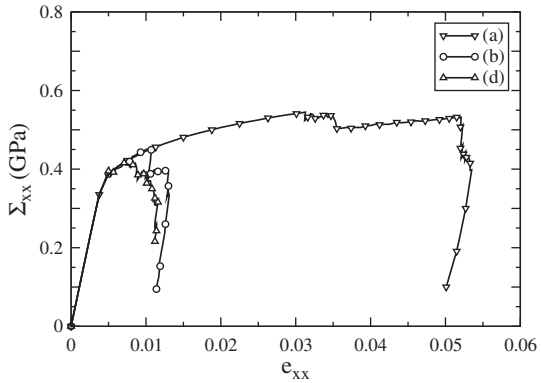

Fig. 5. Macroscopic stress–strain response in uniaxial tension for microstructural domains (a), (b), and (d) of Fig. 4.

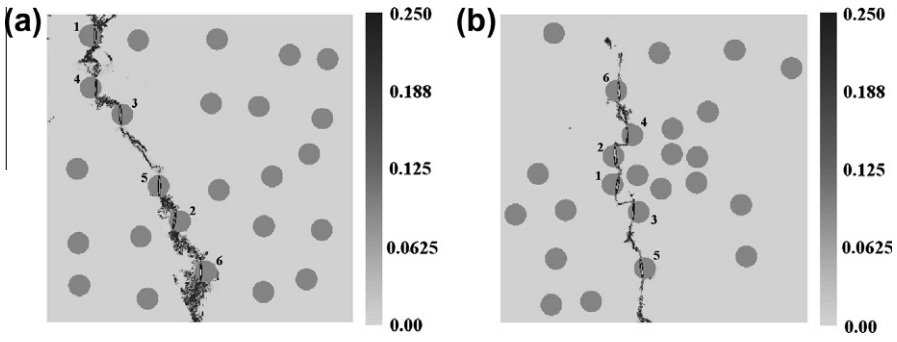

Fig. 6. Contour plots of void volume fraction at final stages of fracture, showing the fracture path, for microstructural domains (a) and (b) of Fig. 4.

Table 5
Simulated strain to failure and maximum stress for microstructural domains of Fig. 4.

Cases	κ	ι	σ_{max} (MPa)	ϵ_{fail}
(a)	4.18	0.632	545	0.049
(b)	8.25	0.771	452	0.011
(c)	6.01	0.800	456	0.009
(d)	4.12	0.505	416	0.010
(e)	4.36	0.690	443	0.013

indicator of ductility, rather than the number of inclusions. The sensitivity study is further enabled by perturbing the morphology of three microstructural domains in Fig. 4 and subsequent simulation. The changes include decreasing the minimum permissible distance (MPD) of microstructure (a) from 0.05 to 0.01, which results in a 1.3% increase in ι (0.632 → 0.640). This change causes a significant reduction of ϵ_{fail} from 4.9% to 2.5%, indicating high sensitivity to ι for low level of clustering. Next, microstructures (b) and (c) are perturbed by increasing the minimum permissible distance within the clusters (MPD-CL) from 0.005 to 0.010. This results in a 4.0% reduction of ι for microstructure (b) (0.771 → 0.740) and 6.4% reduction for microstructure (c) (0.800 → 0.749). Correspondingly, ϵ_{fail} increases by 9.1% for microstructure (b) and 11.1% for microstructure (c). The sensitivity of strain to failure ϵ_{fail} to clustering is lower in this range of clustering, as observed from Fig. 7 as well.

The functional dependence of ϵ_{fail} on ι is shown in Fig. 7. The strain to failure is very high for homogeneous distributions with lower ι. However, a small departure from the homogeneity yields a sharp reduction in ductility due to perturbation of local stresses in the microstructure. The sensitivity of ϵ_{fail} to clustering decreases slowly with increasing levels of clustering. A relation between ι and ϵ_{fail} is derived from a least square fit of the data in Fig. 7 with a correlation coefficient of $R^2 = 0.962$, as:

$$\epsilon_{fail} = F_1(\iota) = \frac{9.50\iota - 5.91}{\iota - 0.632} \times 10^{-3} \tag{40}$$

3.2.3. Sensitivity to inclusion shape and orientation

LE-VCFEM simulations of microstructural domains (d) and (e) in Fig. 4 are conducted to investigate the influence of inclusions shape and orientation on ϵ_{fail}. Corresponding maximum stress and strain to failure values are given in Table 5. The macroscopic stress–strain response for microstructure (d) is also shown in Fig. 5. Strain to failure ϵ_{fail} as a function of ι is plotted in Fig. 8 (striped diamond marker) and compared with that for the circular inclusions (black dots). Results for a distribution of elliptical inclusions, obtained by an orientation perturbation in microstructure (d) (25 inclusions are oriented at angles between −45° and +45° with respect to the horizontal axis) is also shown.

The value of ϵ_{fail} for microstructure (d) is 0.010, which is much less than that for identical circular inclusions, for the same level of clustering ι. This points to the fact that clustering alone does not govern ductility; it also depends on some parameters quantifying inclusion morphology. The low value of ϵ_{fail} for microstructure (d) suggests a strong influence of aspect ratio. The difference between ϵ_{fail} values for microstructure (d) (0.010) and another with a slightly perturbed orientation (0.012) demonstrates that orientation also influences strain to failure. The ϵ_{fail} value for microstructure (e) is quite similar to that predicted by Eq. (40). This may be attributed to the low aspect ratios of inclusions that actually cracked during the simulation, thus reducing the importance of shape and orientation effects.

Additional studies are conducted to quantify the effects of shape and orientation on ductility. To quantify the effect of shape, additional microstructural domains are generated by perturbing the inclusion aspect ratio of microstructure (d) in

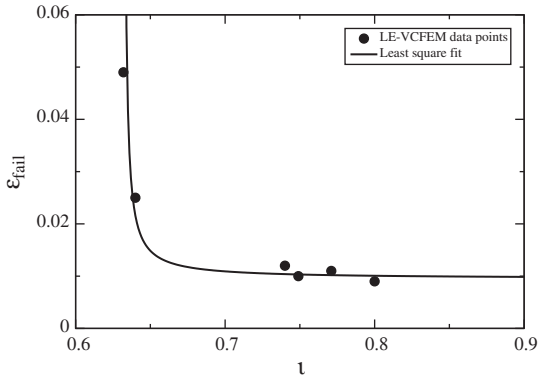

Fig. 7. Correlation between the strain to failure ϵ_{fail} and cluster contour index ι for microstructural domains with different spatial distributions of circular inclusions.

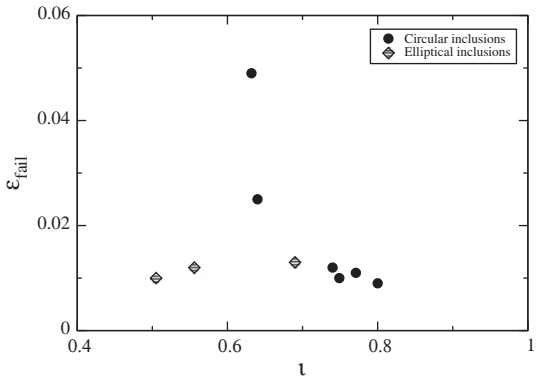

Fig. 8. Correlation between the strain to failure ϵ_{fail} and cluster contour index ι for microstructural domains with different inclusion shapes and orientations. Results of Fig. 7 are also shown for comparison.

Fig. 4, while keeping the same distribution and orientation. Fig. 9 shows the functional dependence of ϵ_{fail} on inclusion roundness ρ, defined as $\rho = \frac{4A}{\pi d_{max}^2}$, where d_{max} is the maximum distance between two points in an inclusion and A is its area. For elliptical inclusions, d_{max} is taken as the major axis and $\rho = b/a$ is the inverse of the aspect ratio. A least square fit of the results of Fig. 9 with a correlation coefficient $R^2 = 0.973$, yields an exponential relation between ϵ_{fail} and ρ as:

$$\epsilon_{fail} = F_2(\rho) = \exp(4.38\rho) \times 10^{-3} \tag{41}$$

The function is plotted with a solid line in Fig. 9. Results show that ϵ_{fail} is quite sensitive to the inclusion aspect ratio for the entire range considered. This suggests that processes like spheroidization can have a significant impact on the ductility of a metal or alloy. Changing the aspect ratio is an efficient way of increasing ductility for materials with non-uniform dispersion, rather than by modifying the level of clustering.

To study the influence of inclusion orientation on ductility, microstructural domains are generated by perturbing the inclusion orientations of microstructure (d) in Fig. 4 with a hard core distribution. All inclusions have the same orientation θ with respect to the horizontal axis. The MPD is also adjusted so that the cluster contour index remains constant at a value $\iota = 0.505$. Fig. 10 shows the correlation between ϵ_{fail} and θ. A least square fit with a correlation coefficient $R^2 = 0.964$ results in a quadratic θ function of the form:

$$\epsilon_{fail} = F_3(\theta) = (11.5 + 7.63\cos\theta - 19.6\cos^2\theta) \times 10^{-2} \tag{42}$$

This function is plotted in Fig. 10. The results show that ϵ_{fail} is significantly reduced when the loading direction is parallel to the major axis of the inclusions.

3.2.4. Sensitivity to inclusion volume fraction

The inclusion volume fraction V_f is generally known to be a determinant of the ductility. Composites or alloys with higher inclusion content have lower strain to failure. The inclusion volume fraction can change, both due to a change in number of

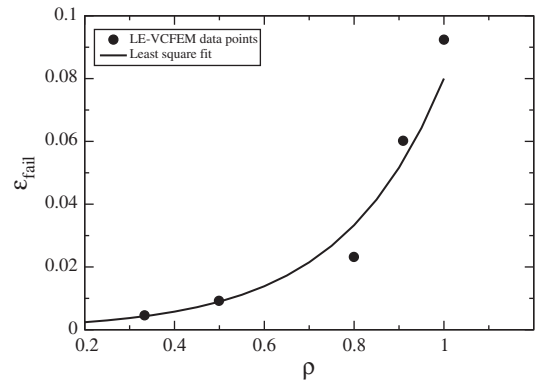

Fig. 9. Correlation between the strain to failure ϵ_{fail} and inclusion roundness ρ for microstructural domains having the same inclusion spatial distribution and orientation, but with different aspect ratios.

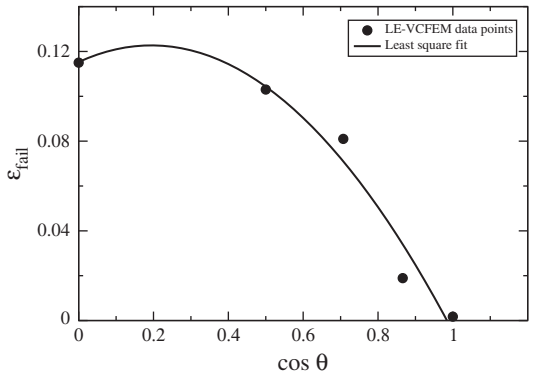

Fig. 10. Correlation between strain to failure ϵ_{fail} and inclusion orientation θ for microstructural domains with inclusions of identical shapes, but with different orientations.

inclusions or due to varying inclusion size. To understand the effect of inclusion volume fraction V_f on strain to failure, microstructural domains with varying area fractions are generated by perturbing the microstructure (b) of Fig. 4.

In the first case, four microstructural domains with increasing sizes of identical circular inclusions are generated. The corresponding four volume fractions are: (i) 5%, (ii) 7.5%, (iii) 10%, and (iv) 12.5%, respectively. The cluster contour index is kept constant at $\iota = 0.740$. Fig. 11 shows the correlation between ϵ_{fail} and the normalized inclusion size $\bar{d} = \frac{d}{L_{MD}}$, with fixed ι and number of inclusions. For a circular inclusion, d is the diameter, while for elliptical inclusions $d = \sqrt{\frac{4A}{\pi}}$. $L_{MD} = \sqrt{A_{MD}}$ is the length scale of the microstructural domain of area A_{MD}. A least square method with a correlation coefficient $R^2 = 0.988$ yields a functional of the form:

$$\epsilon_{fail} = F_4(\bar{d}) = 2.33\bar{d}^{-4.14} \times 10^{-7} \tag{43}$$

This function is plotted in Fig. 11.

Next, the inclusion volume fraction is altered by changing the number of inclusions. Four microstructural domains are generated by adding/removing inclusions to the hard core region or the cluster of microstructure (b) of Fig. 4. Table 6 gives

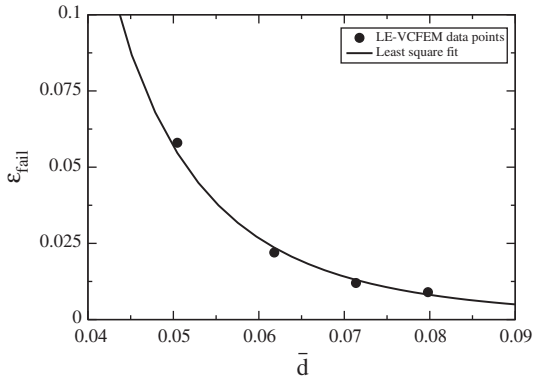

Fig. 11. Correlation between normalized inclusion size $\bar{d}$ and simulated strain to failure ϵ_{fail} for microstructural domains having 25 identical circular inclusions and a cluster contour index $\iota = 0.740$.

Table 6
Parameters, cluster contour index and simulated strain to failure of microstructural domains having different inclusion volume fraction and/or number of inclusions.

Cases	V_f (%)	#CL	#INC	a	b	#INC-CL	ι	ϵ_{fail}
(a)	10	1	25	0.0714	0.0714	11	0.740	0.012
(b)	7.6	1	19	0.0714	0.0714	5	0.745	0.022
(c)	12.4	1	31	0.0714	0.0714	17	0.738	0.009
(d)	7.6	1	19	0.0714	0.0714	11	0.792	0.012
(e)	12.4	1	31	0.0714	0.0714	11	0.704	0.012

the parameters used to generate these microstructural domains (b–e), as well as the cluster contour index and the simulated strains to failure. Characteristics of a reference microstructure (a) containing 25 inclusions are also provided for comparison.

The cluster contour index ι has been demonstrated to be a good measure of clustering for constant inclusion size and volume fraction. However, results in Table 6 show that for similar values of ι, different volume fraction of identical inclusions can lead to significantly different values of ϵ_{fail}. This indicates that ϵ_{fail} depends on both volume fraction V_f and clustering. Hence the dependence of ϵ_{fail} on ι alone in Eq. (40) is augmented by a composite function of both ι and V_f. For microstructures (a), (d) and (e), the identical value of $\epsilon_{fail} = 0.012$ yields a linear relation between V_f and ι as $\iota = 0.929 - 1.83V_f$. Consequently, ϵ_{fail} can be expressed as a function of $\tilde{f} = \frac{\iota}{0.929-1.83V_f}$. A least square fit of results in Table 6 and Fig. 7 (correlation coefficient $R^2 = 0.755$) yields the function:

$$\epsilon_{fail} = F_5(\tilde{f}) = \frac{8.63\tilde{f} - 6.94}{\tilde{f} - 0.848} \times 10^{-3} \tag{44}$$

Eq. (44) is plotted as the solid line in Fig. 12.

3.2.5. Morphological parameter based ductility model

Based on the sensitivity studies, a ductility model is proposed for materials with identical inclusions that have identical orientations. A separation of variables is assumed in the functional form of strain to failure as:

$$\epsilon_{fail} = F(\iota, \rho, \theta, \bar{d}, V_f) = F_\rho(\rho)F_\theta(\theta)F_{\bar{d}}(\bar{d})F_{\tilde{f}}(\tilde{f}) \tag{45}$$

Eq. (45) implies weak coupling between the variables ι, ρ, θ, $\bar{d}$ and V_f. Hence, the functions $F_\rho(\rho)$, $F_\theta(\theta)$, $F_{\bar{d}}(\bar{d})$ and $F_{\tilde{f}}(\tilde{f})$ independently represent the effects of inclusion shape, orientation, size and clustering respectively. Each of these functions can be identified with the individual forms derived in Eqs. (41)–(44), i.e.

$$F_\rho(\rho) = C_1 \exp(4.38\rho)$$
$$F_\theta(\theta) = C_2(11.5 + 7.63\cos\theta - 19.6\cos^2\theta)$$
$$F_{\bar{d}}(\bar{d}) = C_3\bar{d}^{-4.14}$$
$$F_{\tilde{f}}(\tilde{f}) = C_4\frac{8.63\tilde{f} - 6.94}{\tilde{f} - 0.848}$$

The coefficient product $C = \prod_{i=1}^{4} C_i$ is calibrated from morphological parameter data and ϵ_{fail} for the microstructure (d) of Fig. 4. For inclusions that are randomly oriented, the function $F_\theta|_{\text{random }\theta} \approx C_2$ with no orientation dependence. The coefficient is calibrated to be $C = 2.25 \times 10^{-10}$. Thus the strain to failure is related to morphological parameters as:

$$\epsilon_{fail} = 2.25(11.5 + 7.63\cos\theta - 19.6\cos^2\theta)\frac{e^{4.38\rho}}{\bar{d}^{4.14}}\left(\frac{8.63\tilde{f} - 6.94}{\tilde{f} - 0.848}\right) \times 10^{-10} \tag{46}$$

For microstructural domains with randomly oriented inclusions F_θ is a constant. A subset of the model in Eq. (46) can be derived for this case as:

$$\epsilon_{fail} = 2.25\frac{e^{4.38\rho}}{\bar{d}^{4.14}}\left(\frac{8.63\tilde{f} - 6.94}{\tilde{f} - 0.848}\right) \times 10^{-10} \tag{47}$$

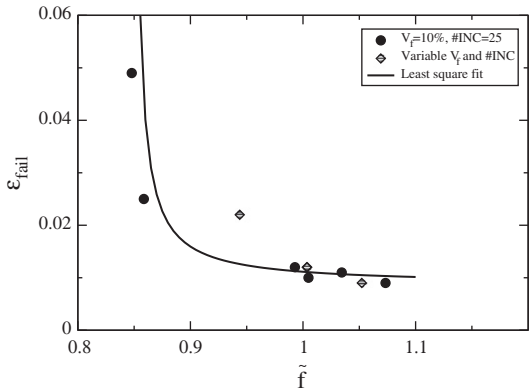

Fig. 12. Correlation between $\tilde{f}$ and strain to failure ϵ_{fail} for the microstructural domains in Table 6 and Fig. 7.

This predictive model for strain to failure is used in the second part of this paper to estimate ϵ_{fail} of microstructural domains obtained from micrographs of a cast aluminum alloy.

3.3. Effect of material properties on ductility

The effect of matrix and inclusion material properties on strain to failure is studied in this section. LE-VCFEM simulations of microstructure (e) in Fig. 4 are undertaken for different values of matrix work-hardening exponent, matrix yield stress and failure strength of inclusions.

3.3.1. Sensitivity to matrix work-hardening exponent and yield stress

The post-yield behavior of the aluminum matrix is represented by the power law Eq. (39) in which yield stress σ_y and hardening exponent N are two important parameters. These properties can be modified by heat treatment, designed to improve the microstructural morphology. Hence, they are implicitly dependent on morphological parameters discussed in Section 3.2.

Table 7 lists the different sets of matrix properties (three values of N and four values of σ_y), used for the LE-VCFEM micromechanical analyses. Macroscopic stress–strain plots, obtained with each set of properties are shown in Figs. 13 and 14. Results in Fig. 13 show that strain to failure is rather insensitive to the hardening exponent, even though the post-yield matrix behavior is significantly altered by a change in N (not shown). The range of work-hardening coefficient N considered in this paper does not result in significant changes in the overall work-hardening response of the heterogeneous domain. The computed strains to failure result from differences in the local distributions of stresses, strains and damage in the microstructure due to the local matrix work-hardening, as opposed to the overall work-hardening behavior. For the microstructure and material properties considered, strain to failure is found to be more sensitive to the value of yield stress σ_y. Fig. 14 reveals that increasing σ_y results in much lower ϵ_{fail}. This is explained by an increase of local stresses in the inclusions that results in earlier inclusion cracking. The reduction of ϵ_{fail} is accompanied by an increase in the maximum tensile strength. The results suggest that reducing the yield stress to get a better strain to failure is not a suitable choice when maximum tensile strength is an important design parameter.

3.3.2. Sensitivity to characteristic inclusion strength

The characteristic strength of inclusions σ_w in the cracking probability model of Eq. (2) depends on the type of material, defects per unit volume, as well as the quality of the inclusion–matrix interface. Two types of inclusions are considered in this study, viz. silicon carbide and silicon inclusions, having a strength σ_w of 500 MPa and 680 MPa respectively. The Young's modulus of silicon carbide and silicon are 427 GPa and 165 GPa, and the Poisson's ratio ν is set to 0.17. The fracture probability P^{cr}_{frag} is set to 95%. Matrix properties are those used in Section 3.2. The macroscopic stress–strain plots are shown in Fig. 15. Increasing σ_w significantly increases both strain to failure and the maximum tensile stress. Nevertheless, materials having silicon carbide inclusions such as metal matrix composites are obtained by processes that affect not only the

Table 7
Different sets of matrix properties used for the sensitivity analysis.

Set	1	2	3	4	5	6
σ_y (MPa)	340	340	340	240	290	390
N	0.135	0.180	0.080	0.135	0.135	0.135

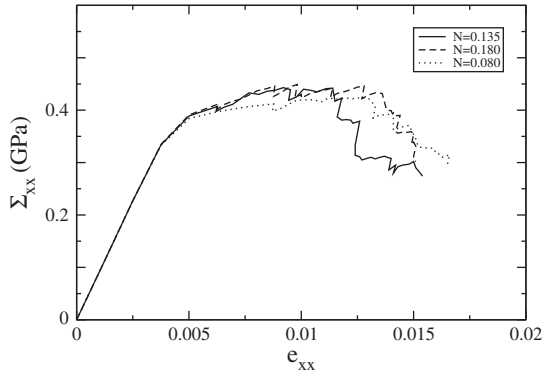

Fig. 13. Macroscopic stress–strain response in uniaxial tension of microstructural domain (e) of Fig. 4 for different values of the matrix work-hardening exponent N.

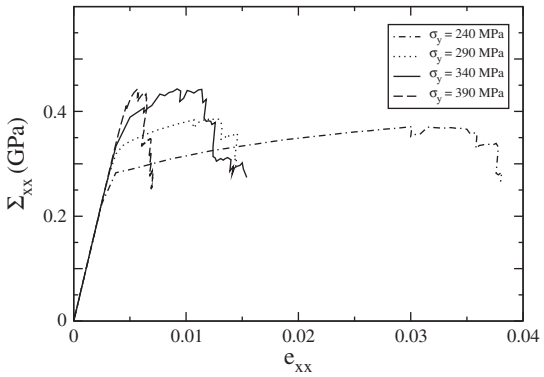

Fig. 14. Macroscopic stress–strain response in uniaxial tension of microstructural domain (e) of Fig. 4 for different values of the matrix yield stress σ_y.

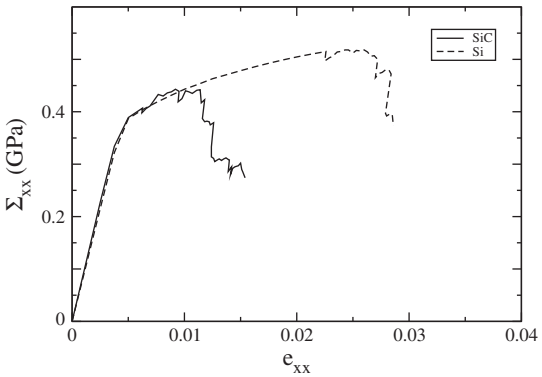

Fig. 15. Macroscopic stress–strain response in uniaxial tension of microstructural domain (e) of Fig. 4 for two different types of inclusion.

inclusion properties, but also the post-yield behavior of the matrix and the distribution of second phase inclusions. As a result, silicon carbide reinforced aluminum composites may have a better strain to failure than a cast aluminum alloy containing eutectic silicon inclusions depending on the distribution and shape of inclusions and post-yield behavior of the matrix.

4. Conclusions

In this first of a two part paper on ductile fracture in heterogeneous materials, extensive microstructure based sensitivity studies are conducted to quantify the effects of loading rates, microstructural morphology and material properties on strain to failure. The locally enhanced VCFEM (LE-VCFEM) for rate-dependent porous elastic–viscoplastic materials is used for two-dimension micromechanical analyses of rate-dependent ductile fracture. The strain to failure is governed by damage nucleation due to inclusion cracking that is followed by damage propagation by void nucleation, growth and coalescence in the matrix. This is readily simulated by LE-VCFEM with good accuracy and efficiency. Strain to failure is found to be very sensitive to the loading rate, microstructure morphology, and material properties of the matrix and inclusions.

High applied strain rates result in early cracking of inclusions. For a uniform material with a single inclusion in the microstructural domain, this leads to an increase of strain to failure due to redistribution of micro-stresses in the matrix and inclusion. This causes a delay in plastic response and a reduction in void evolution rate in the neighborhood of the crack. However, this inference cannot be generalized to more complex microstructures, in which early cracking may have different influence on the overall ductile behavior. Strain to failure of heterogeneous alloys is very sensitive to the inclusion morphology and orientation. Large inclusions of high aspect ratio that are oriented along the loading axis are ideal sites for damage nucleation. The exponential and power law correlations found between strain to failure and inclusion aspect ratio and size respectively delineate this strong sensitivity. On the other hand, damage growth and coalescence in the matrix is affected by the spatial distribution of inclusions rather than by their morphology. Microstructural domains with high levels of clustering have significantly lower strain to failure than those with uniform inclusion distribution. An asymptotic correlation between strain to failure and clustering is found from the sensitivity analysis. This implies a reduction in sensitivity with increasing level of clustering. Based on the sensitivity study, a model is proposed for strain to failure, incorporating the effects of clustering, volume fraction, orientation, shape, size and orientation of inclusions.

The sensitivity analysis also shows that the matrix yield stress and the inclusions failure strength are important determinants of ductility. An increase in the matrix yield stress leads to an increase of the maximum tensile stress that is accompanied by a much lower ductility. The matrix work-hardening exponent on the other hand does not have much effect on ductility for the microstructure and material properties considered in this work. Additionally, strain to failure is found to be very sensitive to the failure strength of inclusions. It is important that a material designer considers both microstructural morphology and material properties in optimizing ductility. In part 2 of this paper, the model for strain to failure developed in part 1 is used to successfully predict strain to failure of actual microstructures taken from micrographs of an aluminum alloy *A356*.

Acknowledgments

This work has been supported by the National Science Foundation NSF Div Civil and Mechanical Systems Division through the GOALI Grant No. CMS-0308666 (Program Director: Dr. G. Paulino), by the Department of Energy Aluminum Visions Program through Grant No. A5997 and by the Army Research Office through Grant No. DAAD19-02-1-0428 (Program Director: Dr. B. Lamattina). This sponsorship is gratefully acknowledged. The authors are grateful to Drs. Steve Harris, John Allison, Xuming Su, and James Boileau of Ford Research Laboratory for invaluable discussions and some micrographs used in this paper. Computer support by the Ohio Supercomputer Center through Grant No. PAS813-2 is also gratefully acknowledged.

Appendix A

The coefficients used in the LE-VCFEM strain update algorithm are given here. A vector $\{\mathbf{H}\}$ is used for compact representation of the state variables f and σ_0, i.e.

$$\begin{Bmatrix} H^1 \\ H^2 \end{Bmatrix} = \begin{Bmatrix} f \\ \sigma_0 \end{Bmatrix} \quad \text{and} \quad \begin{Bmatrix} \Delta H^1 \\ \Delta H^2 \end{Bmatrix} = \begin{Bmatrix} (1-f)\Delta\epsilon_p + A\Delta\bar{\epsilon}^p_M \\ h\Delta\bar{\epsilon}^p_M \end{Bmatrix}$$

where

$$\Delta\bar{\epsilon}^p_M = \frac{-p\Delta\epsilon_p + q\Delta\epsilon_q}{(1-f)\bar{\sigma}_M}$$

The coefficients A_{ij} and b_i are obtained following a linearization technique similar to that in [46], but applied to the rate-dependent porous plasticity strain update algorithm. All the quantities are evaluated at the end of the increment. Repeated indices indicates a summation.

$$A_{11} = \frac{\partial\phi^{vp}}{\partial q} + \Delta\epsilon_p \frac{\partial^2\phi^{vp}}{\partial H^\alpha \partial q}\frac{\partial H^\alpha}{\partial\Delta\epsilon_p} + \Delta\epsilon_q \frac{\partial^2\phi^{vp}}{\partial H^\alpha \partial p}\frac{\partial H^\alpha}{\partial\Delta\epsilon_p}$$

$$A_{12} = \frac{\partial\phi^{vp}}{\partial p} + \Delta\epsilon_p \frac{\partial^2\phi^{vp}}{\partial H^\alpha \partial q}\frac{\partial H^\alpha}{\partial\Delta\epsilon_q} + \Delta\epsilon_q \frac{\partial^2\phi^{vp}}{\partial H^\alpha \partial p}\frac{\partial H^\alpha}{\partial\Delta\epsilon_q}$$

$$A_{13} = \Delta\epsilon_p\left(\frac{\partial^2\phi^{vp}}{\partial p\partial q}\frac{\partial p}{\partial\Delta\sigma_{33}} + \frac{\partial^2\phi^{vp}}{\partial q^2}\frac{\partial q}{\partial\Delta\sigma_{33}} + \frac{\partial^2\phi^{vp}}{\partial H^\alpha\partial q}\frac{\partial H^\alpha}{\partial\Delta\sigma_{33}}\right) + \Delta\epsilon_q\left(\frac{\partial^2\phi^{vp}}{\partial p^2}\frac{\partial p}{\partial\Delta\sigma_{33}} + \frac{\partial^2\phi^{vp}}{\partial q\partial p}\frac{\partial q}{\partial\Delta\sigma_{33}} + \frac{\partial^2\phi^{vp}}{\partial H^\alpha\partial p}\frac{\partial H^\alpha}{\partial\Delta\sigma_{33}}\right)$$

$$b_1 = -\left(\Delta\epsilon_p\frac{\partial\phi^{vp}}{\partial q} + \Delta\epsilon_q\frac{\partial\phi^{vp}}{\partial p}\right)$$

$$A_{21} = -\Delta t\left(\frac{\partial\dot{\lambda}}{\partial H^\alpha}\frac{\partial\phi^{vp}}{\partial q} + \dot{\lambda}\frac{\partial^2\phi^{vp}}{\partial H^\alpha\partial q}\right)\frac{\partial H^\alpha}{\partial\Delta\epsilon_p}$$

$$A_{22} = 1 - \Delta t\left(\frac{\partial\dot{\lambda}}{\partial H^\alpha}\frac{\partial\phi^{vp}}{\partial q} + \dot{\lambda}\frac{\partial^2\phi^{vp}}{\partial H^\alpha\partial q}\right)\frac{\partial H^\alpha}{\partial\Delta\epsilon_q}$$

$$A_{23} = -\Delta t\left(\frac{\partial\dot{\lambda}}{\partial p}\frac{\partial p}{\partial\Delta\sigma_{33}} + \frac{\partial\dot{\lambda}}{\partial q}\frac{\partial q}{\partial\Delta\sigma_{33}} + \frac{\partial\dot{\lambda}}{\partial H^\alpha}\frac{\partial H^\alpha}{\partial\Delta\sigma_{33}}\right)\frac{\partial\phi^{vp}}{\partial q} - \Delta t\dot{\lambda}\left(\frac{\partial^2\phi^{vp}}{\partial p\partial q}\frac{\partial p}{\partial\Delta\sigma_{33}} + \frac{\partial^2\phi^{vp}}{\partial q^2}\frac{\partial q}{\partial\Delta\sigma_{33}} + \frac{\partial^2\phi^{vp}}{\partial H^\alpha\partial q}\frac{\partial H^\alpha}{\partial\Delta\sigma_{33}}\right)$$

$$b_2 = -\left(\Delta\epsilon_q - \Delta t\dot{\lambda}\frac{\partial\phi^{vp}}{\partial q}\right)$$

$$A_{31} = \Delta\epsilon_q\left(-\frac{1}{3}\frac{1}{\partial\phi^{vp}/\partial q}\frac{\partial^2\phi^{vp}}{\partial H^\alpha\partial p}+\frac{1}{3}\frac{\partial\phi^{vp}/\partial p}{(\partial\phi^{vp}/\partial q)^2}\frac{\partial^2\phi^{vp}}{\partial H^\alpha\partial q}\right)\frac{\partial H^\alpha}{\partial\Delta\epsilon_p}$$

$$A_{32} = -\frac{1}{3}\frac{\partial\phi^{vp}/\partial p}{\partial\phi^{vp}/\partial q}+\frac{3}{2q}\sigma'_{33}+\Delta\epsilon_q\left(-\frac{1}{3}\frac{1}{\partial\phi^{vp}/\partial q}\frac{\partial^2\phi^{vp}}{\partial H^\alpha\partial p}+\frac{1}{3}\frac{\partial\phi^{vp}/\partial p}{(\partial\phi^{vp}/\partial q)^2}\frac{\partial^2\phi^{vp}}{\partial H^\alpha\partial q}\right)\frac{\partial H^\alpha}{\partial\Delta\epsilon_q}$$

$$A_{33} = \frac{1}{E}+\Delta\epsilon_q\left(-\frac{1}{3}\frac{1}{\partial\phi^{vp}/\partial q}\left(\frac{\partial^2\phi^{vp}}{\partial p^2}\frac{\partial p}{\partial\Delta\sigma_{33}}+\frac{\partial^2\phi^{vp}}{\partial q\partial p}\frac{\partial q}{\partial\Delta\sigma_{33}}+\frac{\partial^2\phi^{vp}}{\partial H^\alpha\partial p}\frac{\partial H^\alpha}{\partial\Delta\sigma_{33}}\right)\right.$$
$$\left.+\frac{1}{3}\frac{\partial\phi^{vp}/\partial p}{(\partial\phi^{vp}/\partial q)^2}\left(\frac{\partial^2\phi^{vp}}{\partial p\partial q}\frac{\partial p}{\partial\Delta\sigma_{33}}+\frac{\partial^2\phi^{vp}}{\partial q^2}\frac{\partial q}{\partial\Delta\sigma_{33}}+\frac{\partial^2\phi^{vp}}{\partial H^\alpha\partial q}\frac{\partial H^\alpha}{\partial\Delta\sigma_{33}}\right)+\frac{3}{2q}\frac{\partial\sigma'_{33}}{\partial\Delta\sigma_{33}}-\frac{3}{2q^2}\sigma'_{33}\frac{\partial q}{\partial\Delta\sigma_{33}}\right)$$

$$b_3 = -\left(\frac{1}{E}(\Delta\sigma_{33}-\nu\Delta\sigma_{11}-\nu\Delta\sigma_{22})+\Delta\epsilon_q\left(-\frac{1}{3}\frac{\partial\phi^{vp}/\partial p}{\partial\phi^{vp}/\partial q}+\frac{3}{2q}\sigma'_{33}\right)-\hat{\epsilon}^{constant}\right)$$

with

$$\frac{\partial p}{\partial\Delta\sigma_{33}} = -\frac{1}{3},\quad \frac{\partial q}{\partial\Delta\sigma_{33}} = \frac{3}{2q}\sigma'_{33},\quad \frac{\partial\sigma'_{33}}{\partial\Delta\sigma_{33}} = \frac{2}{3}$$

The state variables derivatives are defined as follows [46]:

$$\frac{\partial H^\alpha}{\partial\Delta\epsilon_p} = c_{\alpha\beta}\left(\frac{\partial\Delta H^\beta}{\partial\Delta\epsilon_p}+K\frac{\partial\Delta H^\beta}{\partial p}\right),\quad \frac{\partial H^\alpha}{\partial\Delta\epsilon_q} = c_{\alpha\beta}\left(\frac{\partial\Delta H^\beta}{\partial\Delta\epsilon_q}-3G\frac{\partial\Delta H^\beta}{\partial q}\right)$$

where $c^{-1}_{\alpha\beta} = \delta_{\alpha\beta}-\frac{\partial\Delta H^\alpha}{\partial H^\beta}$.

Appendix B

The coefficients used for stress update in the displacement-based elements of LE-VCFEM formulation are:

$$A_{11} = \frac{\partial\phi^{vp}}{\partial q}+\Delta\epsilon_p\left(K\frac{\partial^2\phi^{vp}}{\partial p\partial q}+\frac{\partial^2\phi^{vp}}{\partial q\partial H^\alpha}\frac{\partial H^\alpha}{\partial\Delta\epsilon_p}\right)+\Delta\epsilon_q\left(K\frac{\partial^2\phi^{vp}}{\partial p^2}+\frac{\partial^2\phi^{vp}}{\partial p\partial H^\alpha}\frac{\partial H^\alpha}{\partial\Delta\epsilon_p}\right)$$

$$A_{12} = \frac{\partial\phi^{vp}}{\partial p}+\Delta\epsilon_p\left(-3G\frac{\partial^2\phi^{vp}}{\partial q^2}+\frac{\partial^2\phi^{vp}}{\partial q\partial H^\alpha}\frac{\partial H^\alpha}{\partial\Delta\epsilon_q}\right)+\Delta\epsilon_q\left(-3G\frac{\partial^2\phi^{vp}}{\partial q\partial p}+\frac{\partial^2\phi^{vp}}{\partial p\partial H^\alpha}\frac{\partial H^\alpha}{\partial\Delta\epsilon_q}\right)$$

$$b_1 = -\Delta\epsilon_p\frac{\partial\phi^{vp}}{\partial q}-\Delta\epsilon_q\frac{\partial\phi^{vp}}{\partial p}$$

$$A_{21} = -\Delta t\left(K\frac{\partial\dot{\lambda}}{\partial p}+\frac{\partial\dot{\lambda}}{\partial H^\alpha}\frac{\partial H^\alpha}{\partial\Delta\epsilon_p}\right)\frac{\partial\phi^{vp}}{\partial q}-\Delta t\dot{\lambda}\left(K\frac{\partial^2\phi^{vp}}{\partial p\partial q}+\frac{\partial^2\phi^{vp}}{\partial q\partial H^\alpha}\frac{\partial H^\alpha}{\partial\Delta\epsilon_p}\right)$$

$$A_{22} = 1-\Delta t\left(-3G\frac{\partial\dot{\lambda}}{\partial q}+\frac{\partial\dot{\lambda}}{\partial H^\alpha}\frac{\partial H^\alpha}{\partial\Delta\epsilon_q}\right)\frac{\partial\phi^{vp}}{\partial q}-\Delta t\dot{\lambda}\left(-3G\frac{\partial^2\phi^{vp}}{\partial q^2}+\frac{\partial^2\phi^{vp}}{\partial q\partial H^\alpha}\frac{\partial H^\alpha}{\partial\Delta\epsilon_q}\right)$$

$$b_2 = -\Delta\epsilon_q+\Delta t\dot{\lambda}\frac{\partial\phi^{vp}}{\partial q}$$

References

[1] Edelson BI, Baldwin Jr WM. The effect of second phases on the mechanical properties of alloys. Trans ASM 1962;55:230–50.
[2] Meyers CW, Saigal A, Berry JT. Fracture related properties of A357-T6 cast alloy and their interrelation with microstructure. AFS Trans 1983;35:281–8.
[3] Hahn GT, Rosenfield AR. Metallurgical factors affecting fracture toughness of aluminum alloys. Metall Trans A 1975;6A(4):653–68.
[4] Gangulee A, Gurland J. On the fracture of silicon particles in aluminum–silicon alloys. Trans Met Soc AIME 1967;239(2):269–72.
[5] Frederick SF, Bailey WA. The relation of ductility to dendrite cell size in cast Al–Si–Mg alloy. Trans Met Soc AIME 1968;242(10):2063–7.
[6] Caceres C, Griffiths J. Damage by the cracking of silicon particles in an Al–7Si–0.4Mg casting alloy. Acta Mater 1996;44:25–33.
[7] Llorca J, Martin A, Ruiz J, Elices M. Particulate fracture during deformation of a spray formed metal–matrix composite. Metall Trans A 1993;24A:1575–88.
[8] Guiglionda G, Poole WJ. The role of damage on the deformation and fracture of Al–Si eutectic alloys. Mater Sci Engng 2002;A336:159–69.

[9] Yang J, Cady C, Hu MS, Zok F, Methrabian R, Evans G. Effects of damage on the flow strength and ductility of a ductile Al alloy reinforced with SiC particulates. Acta Metall Mater 1990;38(12):2613–9.
[10] Lloyd DJ. Aspects of fracture in particulate reinforced metal matrix composites. Acta Metall Mater 1991;39(1):59–71.
[11] Li M, Ghosh S, Richmond O, Weiland H, Rouns T. Three dimensional characterization and modeling of particle reinforced metal matrix composites part I: quantitative description of microstructural morphology. Mater Sci Engng 1999;265:153–73.
[12] Li M, Ghosh S, Richmond O, Weiland H, Rouns T. Three dimensional characterization and modeling of particle reinforced metal matrix composites part II: damage characterization. Mater Sci Engng 1999;266:221–40.
[13] Caceres C, Davidson C, Griffiths J. The deformation and fracture behaviour of an Al–Si–Mg casting alloy. Mater Sci Engng 1995;A197:171–9.
[14] Caceres C, Griffiths J, Reiner P. The influence of microstructure on the bauschinger effect in an Al–Si–Mg casting alloy. Acta Mater 1996;44:15–23.
[15] Caceres C. Particle cracking and the tensile ductility of a model Al–Si–Mg composite system. Aluminum Trans 1999;1:1–13.
[16] Wang Q, Caceres C, Griffiths J. Damage by eutectic particle cracking in aluminum casting alloys A356/357. Metall Mater Trans A 2003;34A:2901–12.
[17] Wang Q. Microstructural effects on the tensile and fracture behavior of aluminum casting alloys A356/357. Metall Mater Trans A 2003;34A:2887–99.
[18] Ghosal A, Narasimhan R. Mixed-mode fracture initiation in a ductile material with a dual population of second-phase particles. Mater Sci Engng 1996;A211:117–27.
[19] Steglich D, Brocks W. Micromechanical modeling of the behavior of ductile materials including particles. Comput Mater Sci 1997;9:7–17.
[20] Lim L, Dunne F. Modeling void nucleation and growth processes in a particle-reinforced metal matrix composite material. Comput Mater Sci 1996;5:177–86.
[21] Negre P, Steglich D, Brocks W, Kocak M. Numerical simulation of crack extension in aluminium welds. Comput Mater Sci 2003;28:723–31.
[22] Huber G, Brechet Y, Pardoen T. Predictive model for void nucleation and void growth controlled ductility in quasi-eutectic cast aluminium alloys. Acta Mater 2005;53:2739–49.
[23] Llorca J, Gonzalez C. Microstructural factors controlling the strength and ductility of particle-reinforced metal–matrix composites. J Mech Phys Solids 1998;46:1–28.
[24] Llorca J, Segurado J. Three-dimensional multiparticle cell simulations of deformation and damage in sphere-reinforced composites. Mater Sci Engng 2004;A365:267–74.
[25] Kiser M, Zok F, Wilkinson D. Plastic flow and fracture of a particulate metal matrix composite. Acta Metall Mater 1996;9:3465–76.
[26] Moorthy S, Ghosh S. Adaptivity and convergence in the Voronoi Cell finite element model for analyzing heterogeneous materials. Comput Method Appl Mech Engng 2000;185:37–74.
[27] Ghosh S, Ling Y, Majumdar B, Kim R. Interfacial debonding analysis in multiple fiber reinforced composites. Mech Mater 2000;32:561–91.
[28] Li S, Ghosh S. Extended Voronoi Cell finite element model for multiple cohesive crack propagation in brittle materials. Int J Numer Methods Engng 2006;65:1028–67.
[29] Li S, Ghosh S. Multiple cohesive crack growth in brittle materials by the extended Voronoi Cell finite element model. Int J Fract 2006;141:373–93.
[30] Moorthy S, Ghosh S. A Voronoi Cell finite element model for particle cracking in elastic–plastic composite materials. Comput Method Appl Mech Engng 1998;151:377–400.
[31] Ghosh S, Moorthy S. Particle fracture simulation in non-uniform microstructures of metal–matrix composites. Acta Mater 1998;46:965–82.
[32] Hu C, Ghosh S. Locally enhanced Voronoi Cell finite element model (LE-VCFEM) for simulating evolving fracture in ductile microstructures containing inclusions. Int J Numer Methods Engng 2008;76:1955–92.
[33] Li M, Ghosh S, Richmond O. An experimental–computational approach to the investigation of damage evolution in discontinuously reinforced aluminum matrix composite. Acta Mater 1999;47:3515–32.
[34] Ghosh S, Mukhopadhyay S. A two dimensional automatic mesh generator for finite element analysis of random composites. Comput Struct 1991;41:245–56.
[35] Zienkiewicz O, Zhu J. The superconvergent patch recovery and a posteriori error estimates. Part 1: the recovery technique. Int J Numer Methods Engng 1992;33:1331–64.
[36] Chu CC, Needleman A. Void nucleation effects in biaxially stretched sheets. J Engng Mater Technol 1980;102:249–56.
[37] Tvergaard V, Needleman A. Analysis of cup-cone fracture in a round tensile bar. Acta Metall 1984;32:157–69.
[38] Tvergaard V, Needleman A. Effect of nonlocal damage in porous plastic solids. Int J Solids Struct 1995;32:1063–77.
[39] Gurson A. Continuum theory of ductile rupture by void nucleation and growth. J Engng Mater Trans ASME 1977;99:2–15.
[40] Tvergaard V. Influence of voids on shear band instabilities under plane strain conditions. Int J Fract Mech 1981;17:389–407.
[41] Perzyna P. Fundamental problems in viscoplasticity. Adv Appl Mech 1966;9:243–377.
[42] Ghosh S, Kikuchi N. An arbitrary Lagrangian–Eulerian finite element method for large deformation analysis of elastic–viscoplastic solids. Comput Method Appl Mech Engng 1991;86:127–88.
[43] Hill R. On constitutive macro-variables for heterogeneous solids at finite strain. Proc Roy Soc Lond 1972;326:131–47.
[44] Kroner E. Statistical modeling. In: Gittus JZJ, editor. Modeling small deformations of polycrystals. London: Elsevier; 1986. p. 229–91.
[45] Green AE, Naghdi PM. A general theory of an elastic–plastic continuum. Arch Ration Mech Anal 1965;18:251–81.
[46] Aravas N. On the numerical integration of a class of pressure-dependent plasticity models. Int J Numer Methods Engng 1987;24:1395–416.
[47] Kwon D, Lee S, Roh B-I. Strain-rate effects on high-temperature fracture behavior of a 2124Al–SiCw composite. Metall Trans A 1993;24A:1125–993.
[48] Ghosh S, Nowak Z, Lee K. Quantitative characterization and modeling of composite microstructures by Voronoi cells. Acta Mater 1997;45:2215–34.
[49] Wray PJ, Richmond O, Morrison HL. Use of the dirichlet tessellation for characterizing and modeling nonregular dispersions of second-phase particles. Metallography 1983;16:39–58.
[50] Pyrz R. Correlation of microstructure variability and local stress field in two-phase materials. Mater Sci Engng 1994;A177:253–9.
[51] Everett RK. Quantification of random fiber arrangements using a radial distribution function approach. J Compos Mater 1996;30(6):748–58.
[52] Ghosh S, Valiveti D, Harris S, Boileau J. A domain partitioning based pre-processor for multi-scale modeling of cast aluminum alloys. Modell Simul Mater Sci Engng 2006;14:1363–96.